

CERAMIC PROCESSING OF A GARNET-BASED SUPERIONIC CONDUCTING
OXIDE: LITHIUM LANTHANUM ZIRCONIUM ALUMINATE

By

Isabel N. David

A THESIS

Submitted to
Michigan State University
in partial fulfillment of the requirements
for the degree of

Materials Science and Engineering - Master of Science

2014

ABSTRACT

CERAMIC PROCESSING OF A GARNET-BASED SUPERIONIC CONDUCTING OXIDE: LITHIUM LANTHANUM ZIRCONIUM ALUMINATE

By

Isabel N. David

Optimizing solid-state batteries will reduce the reliance on fossil fuel for electricity and energy storage technologies. Current energy storage technologies that are used in electric vehicles require secondary batteries with a liquid electrolyte. Safety hazards associated with the degradation of liquid electrolytes can be eliminated if a superionic conducting oxide (SCO) electrolyte were used instead. To match or exceed the current ionic conductivity values of a liquid electrolyte, SCO electrolytes need to be near theoretical density and be thermally and chemically stable in air and against metallic lithium. High-density SCO electrolytes can be produced through optimization of the sintering conditions; i.e., time, temperature, pressure, and chemical composition. Ceramic powder processing optimization of the sintering temperature and sintering mechanism has been shown here to increase the density as well as the Li-ion conductivity in the garnet-based SCO electrolyte $\text{Li}_7\text{La}_3\text{Zr}_2\text{O}_{12}$. It is reported herein that 1) increasing the sintering temperature reduced porosity, impurity phases, and the grain boundary resistance and 2) adding various amounts of a sintering aid, tri-isopropyl borate (TIB), reduced the sintering temperature and still maintained comparable electrochemical properties.

Copyright by
ISABEL N. DAVID
2014

This thesis is dedicated to the network of friends and family that I have come to know and love at or around Michigan State University. My journey as a graduate student has been a series of unfortunate events as well as a tale of great success. It has been a combination of finding out what my deepest passions are in research and realizing that I have one of the strongest support systems I could have ever asked for. I would love to take the time to acknowledge each and every peer, family member and closest friend but I do not have time or space to account for all of their support, love, and encouragement. Suffice it say that I would not have made it to this point in my life without that support. The times I needed a listening ear or a kick in the rear, the moments of weakness that were met with ice cream and hugs, and the true friendship and love I exchanged with many of you. So I dedicate this work to all of you who have supported me through my time at MSU. I give you all due credit for contributing to this work in some very significant ways.

ACKNOWLEDGEMENTS

I would like to thank my advisor and mentor Dr. Jeff Sakamoto for being patient with my early attempts at independent research and pushing me to expect more from myself, when necessary. Without his guidance, encouragement, and research philosophy my view of objective science would still be limited. His laboratory is comprised of a unique mixture of cooperation, acceptance, and hard work. That leads me to acknowledge all of the amazingly kind and inspiring co-workers I've had the honor to work beside: Dr. Ryan Maloney, Dr. Ezhiyl Rangasamy, Dr. Dan Lynam, Dr. Young-Sam Park, Travis Thompson, Dena Shahriari, Alexa Coffman, Yunsung Kim, Asma Sharafi, Regina Garcia, Shaubhik Bhattacharjee. All of you are dedicated researchers that have a long career in science ahead of you. Another mentor during my time at MSU has been Dr. Per Askeland. I would like to thank him for training me on the machines that have merged my scientific curiosity with aesthetic harmony. The tools he has taught me will be important in life as well as my career. Also, Danielle, Donna, Nikki, Jennifer, and Kim from the ChEMs graduate office deserve a special thank you for making my transitions during graduate school possible with their dedicated work ethic, depth of academic bureaucracy knowledge, biggest smiles, and warmest hugs. Outside of the engineering environment, I want to thank my fiancé, Steve for helping me every step of the way and my family for supporting me through all of my decisions. Finally, I would like to thank Dr. Carl Boehlert and Dr. Andre Lee for serving on my committee. You both have guided me and helped me throughout my years at MSU.

TABLE OF CONTENTS

| | |
|---|------|
| LIST OF TABLES..... | viii |
| LIST OF FIGURES..... | xi |
| | |
| 1. Introduction..... | 1 |
| 1.1 Problem statement..... | 1 |
| 1.2 Comparing energy storage technologies..... | 3 |
| 1.3 Supercapacitors, Solid Oxide Fuel cells, and Batteries..... | 5 |
| 1.4 The battery: schematic and operating mechanism..... | 8 |
| 1.5 State of the art batteries..... | 10 |
| 1.6 Inorganic superionic conducting oxide (SCO) electrolytes..... | 15 |
| 1.6.1 Necessary SCO electrolyte performance criteria..... | 16 |
| 1.6.2 Review of SCO electrolytes..... | 16 |
| 1.7 Ceramic processing techniques..... | 22 |
| 1.7.1 Comparison of hot pressing and pressure-less sintering methods..... | 24 |
| 1.7.2 Sintering aids for Liquid-Phase Sintering..... | 25 |
| | |
| 2. Effect of hot pressing temperature on the microstructure and Li-ion transport of $\text{Li}_6\text{La}_3\text{Zr}_2\text{Al}_{0.34}\text{O}_{12}$ | 27 |
| 2.1 Introduction..... | 27 |
| 2.2 Experimental Methods..... | 29 |
| 2.2.1 Powder Preparation and Hot-Pressing Technique..... | 29 |
| 2.2.2 Pellet Characterization..... | 30 |
| 2.3 Results and Discussions..... | 31 |
| 2.3.1 Effect of hot pressing temperature on phase purity and microstructure..... | 31 |
| 2.3.1.1 Anomalous behavior in the 900°C pellet..... | 36 |
| 2.3.2 Electrochemical Impedance Spectroscopy (EIS)..... | 37 |
| 2.4 Conclusion..... | 41 |
| 2.5 Acknowledgements..... | 42 |
| | |
| 3. Liquid phase sintering of $\text{Li}_{6.22}\text{La}_3\text{Zr}_2\text{Al}_{0.26}\text{O}_{12}$ with the sintering aid Tri-isopropyl borate..... | 42 |
| 3.1 Introduction..... | 42 |
| 3.2 Experimental Methods..... | 44 |
| 3.2.1 Powder Preparation and Hot-Pressing Technique..... | 44 |
| 3.2.2 Pellet Characterization..... | 46 |
| 3.3 Results and Discussion..... | 47 |
| 3.3.1 Thermogravimetric analysis (TGA), Differential scanning calorimetry (DSC), and X-Ray Diffraction (XRD)..... | 47 |
| 3.3.2 Density and Microstructural analysis..... | 54 |
| 3.3.3 Electrochemical Impedance spectroscopy (EIS)..... | 58 |
| 3.3.3.1 Effects of the TIB sintering aid..... | 62 |

| | |
|-----------------------|----|
| 3.4 Conclusion..... | 64 |
| 4. Future Works | 65 |
| BIBLIOGRAPHY..... | 68 |

LIST OF TABLES

| | |
|--|----|
| Table 2.1: Microstructural details of hot pressed LLZO pellets..... | 32 |
| Table 2.2: Electrochemical properties of hot pressed LLZO pellets..... | 39 |
| Table 3.1: Electrochemical properties of hot pressed LLZO – X wt% TIB pellets (X =1, 2, and 5 wt %)..... | 62 |

LIST OF FIGURES

| | |
|---|----|
| Figure 1.1: Energy use in the United States in 2011..... | 3 |
| Figure 1.2: Ragone Plot depicting specific energy against specific power for various energy storage technologies. The diagonal lines represent the time of charge for each energy storage technology..... | 4 |
| Figure 1.3: Schematic of a lithium ion battery (LIB)..... | 9 |
| Figure 1.4: Comparison of current and potential battery technologies with their specific energies (Wh kg^{-1}) and prices ($\text{US\$ kWh}^{-1}$) listed..... | 13 |
| Figure 2.1: XRD patterns of the LLZO powder and hot-pressed pellets from 900°C to 1100°C , impurity phases are indicated by: * pyrochlore ($\text{La}_2\text{Zr}_2\text{O}_7$) and \blacklozenge perovskite (LaAlO_3)..... | 32 |
| Figure 2.2: Backscattered electron SEM images of polished a,d) 900°C b,e) 1000°C and c,f) 1100°C pellets..... | 34 |
| Figure 2.3: Secondary electron SEM images of fracture surfaces a,d) 900°C b,e) 1000°C and c,f) 1100°C pellets..... | 34 |
| Figure 2.4: SEM analysis (24,000x) of the 900°C hot-pressed pellet with a) secondary electrons and b) backscattered electrons, arrows point to the film visible on all the internal pores surfaces..... | 35 |
| Figure 2.5: Impedance plot (7 MHz – 1 Hz) of hot-pressed LLZO pellets at various sintering temperatures. Markers indicate experimental data and the solid lines, for the 1000°C and 1100°C pellets, are simulated lines extrapolated from the best-fit line..... | 39 |
| Figure 2.6: Impedance plot of 1000°C (circles) and 1100°C (triangles) hot-pressed LLZO pellets at high frequency. Markers indicate experimental data and the solid lines are simulated lines extrapolated from the equivalent circuit modeling using the equivalent circuit shown here..... | 40 |
| Figure 3.1: Schematic of LLZO + TIB powder synthesis..... | 50 |
| Figure 3.2: Thermogravimetric analysis (green) and Differential scanning calorimetry (blue) on LLZO + 5 wt% TIB in the temperature range 25°C to 1200°C in a nitrogen atmosphere at $5^{\circ}\text{C min}^{-1}$ | 50 |

| | |
|--|----|
| Figure 3.3: Phase diagram for Li ₂ O and B ₂ O ₃ from Sastry <i>et al.</i> | 51 |
| Figure 3.4: X-ray diffraction of the as-synthesized powder (a) and the four samples after the first heat treatment at 450°C. b) Control sample c) 1 wt% TIB d) 2 wt% TIB e)..... | 52 |
| Figure 3.5: XRD of the LLZO + TIB samples after hot pressing at 900°C. a) JCPDS 08-457 b) Pre-sintered LLZO powder c) Control sample d) 1 wt% TIB e) 2 wt% TIB and f) 5 wt% TIB. Impurity phases are indicated by: * pyrochlore (La ₂ Zr ₂ O ₇) and ♦ perovskite (LaAlO ₃) | 53 |
| Figure 3.6: SEM polished surface images (backscattered electrons) at 2000x of a) 0 wt% TIB b) 1 wt% TIB c) 2 wt% TIB and d) 5 wt% TIB..... | 55 |
| Figure 3.7: SEM fracture surface images (secondary electrons) at 1000x of a) 0 wt% TIB b) 1 wt% TIB c) 2 wt% TIB and d) 5 wt% TIB..... | 55 |
| Figure 3.8: SEM fracture surface images (secondary electrons) at 8000x of a) 0 wt% TIB b) 1 wt% TIB c) 2 wt% TIB and d) 5 wt% TIB Electrochemical properties of hot pressed LLZO pellets..... | 56 |
| Figure 3.9: Equivalent circuit model based on work by Huggins <i>et al.</i> (Huggins 2002) R, CPE, and M refer to the resistance, mass transport element, and constant phase element and the subscripts uncomp, geo, gb, int represent uncompensated, geometric dimensions, grain boundary, and interfaces..... | 59 |
| Figure 3.10: Impedance plot (7 MHz – 1 Hz) of hot-pressed LLZO-Xwt% TIB pellets. Markers indicate experimental data and the solid lines, for the X = 1, 2, and 5 wt% TIB, indicate the equivalent circuit modeled line..... | 60 |
| Figure 3.11: Impedance plot of hot-pressed LLZO-Xwt% TIB pellets. Markers indicate experimental data and the solid lines, for the X = 1, 2, and 5 wt% TIB, indicate the equivalent circuit modeled line..... | 61 |

1. Introduction

1.1 Problem statement

Developing new energy storage technologies is critical to secure the future of our electricity supply and to reduce the world's reliance on fossil fuels. We currently rely extensively on energy storage technologies, both in portable forms for communication and international travel, and in stationary forms for supplementing energy grids.(van Vliet *et al.* 2011) These technologies are integrated into a worldwide system that already struggles to meet current demands, much less the increased demands of the future.(Galli *et al.* 2011; Hashmi *et al.* 2011) To improve this system, and to reduce the world's reliance on fossil fuels, the United States (US) and other developed countries around the world are undertaking large-scale endeavors to improve both portable and grid energy storage technologies.

These efforts take the form of three interrelated large scale endeavors: designing an electricity system that combines energy acquisition with energy storage; developing flexible energy storage technologies to deal with the variability of renewable energy acquisition and consumer demand; and promoting the use of electric vehicles that will utilize this grid. The successful implementation of these three endeavors would provide a promising solution based on renewable energy sources and avoid non-renewable fossil fuels.

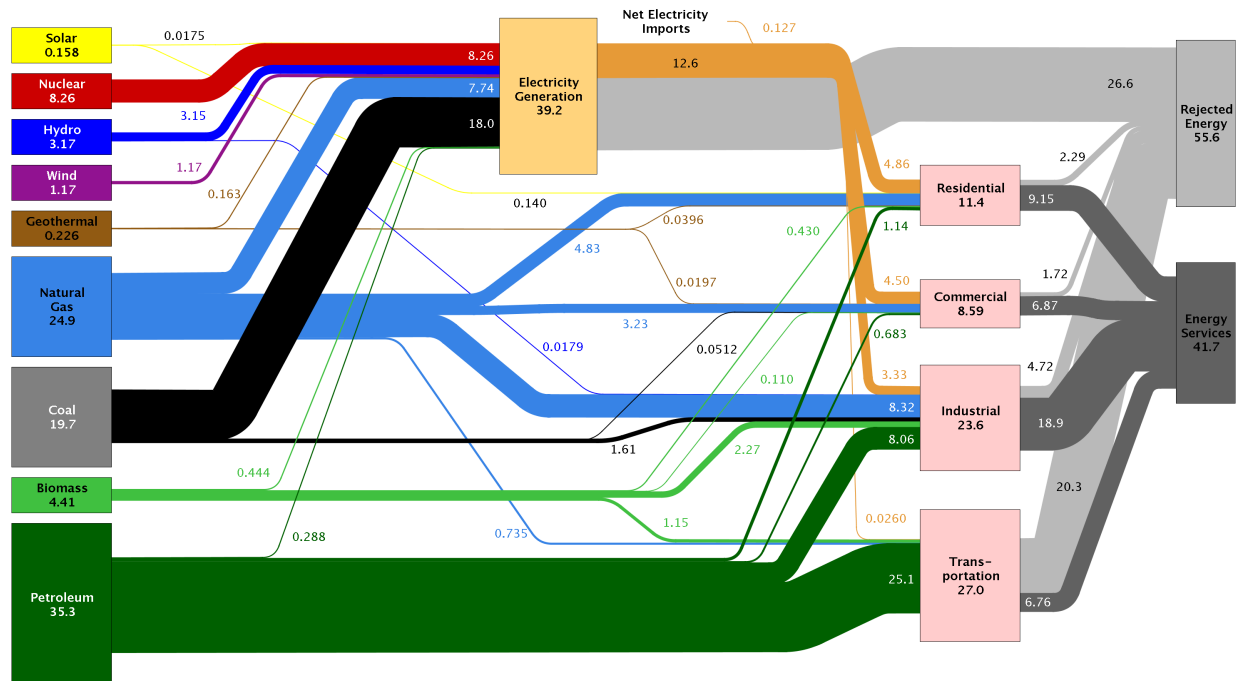
The first endeavor, designing an electricity system that encompasses energy acquisition as well as storage, is already underway in the Netherlands.(Bellekom *et al.* 2012) The Dutch electricity and transport sectors have established the goal of utilizing 10 GW of installed wind energy, as well as manufacturing one million electric vehicles (EVs), by 2020.(Bellekom *et al.* 2012) Use of these vehicles will reduce CO₂ emissions.(Bellekom *et al.* 2012) Bellekom *et al.*

suggest that reducing problems within the entire electricity system can be achieved by combining increased wind power capabilities and EV development: for example, charging thousands of EVs at night would provide an outlet for electricity produced in excess of the total daily demand.(Bellekom *et al.* 2012) A problem with this approach arises, however, in that wind energy runs continuously, but with variable output. This means that suitable energy storage technologies will need to be developed before this approach can be successfully implemented on a large scale.

This leads directly into the second major challenge: developing an electricity system built around flexible energy storage technologies. Such a system would dynamically store energy during low consumption times and draw energy back out as needed to meet peak demand. Implementing such a system would accommodate unpredictable periods of high and low velocity winds. Currently, the extended-range electric automobile is experiencing increased public demand on both technological and economical fronts(Kley *et al.* 2011; Bruce *et al.* 2011), so now is an excellent time for new EVs to gain a foothold in the market.

Progress is already being made on the third endeavor, developing electric vehicles that will feed off this flexible energy grid and reduce dependence on fossil fuels (Figure 1.1). The EVs currently available are still markedly less accessible and less commonly used than traditional automobiles. This can be attributed to their high cost and lack of available charging stations, as well as relatively long charging times, shorter driving ranges, and poor maximum power.(Chu 2007; Bruce *et al.* 2011; Kley *et al.* 2011) The impetus for improved vehicular performance has thus been well established(Chu 2007; van Vliet *et al.* 2010; van Vliet *et al.* 2011; Bruce *et al.* 2011).

Estimated U.S. Energy Use in 2011: ~97.3 Quads



Source: LLNL 2012. Data is based on DOE/EIA-0384(2011), October, 2012. If this information or a reproduction of it is used, credit must be given to the Lawrence Livermore National Laboratory and the Department of Energy, under whose auspices the work was performed. Distributed electricity represents only retail electricity sales and does not include self-generation. EIA reports flows for non-thermal resources (i.e., hydro, wind and solar) in BTU-equivalent values by assuming a typical fossil fuel plant "heat rate." The efficiency of electricity production is calculated as the total retail electricity delivered divided by the primary energy input into electricity generation. End use efficiency is estimated as 80% for the residential, commercial and industrial sectors, and as 25% for the transportation sector. Totals may not equal sum of components due to independent rounding. LLNL-MI-410527

Figure 1.1 Energy use in the United States in 2011. (LLNL 2012)

Research hubs in the US, such as the Joint Center for Energy Storage Research (JCESR) under the US Department of Energy (DoE), have ambitious goals¹ to implement new research methods to advance energy storage technologies.

1.2 Comparing energy storage technologies

A variety of energy storage and conversion technologies have emerged as candidates to help meet these challenges. Supercapacitors, solid oxide fuel cells, and batteries all have the capability of storing energy to different degrees, and each technology has its own advantages and disadvantages with respect to performance, cost, and availability.(Dunn *et al.* 2011; Sakamoto

¹ To pursue advanced scientific research to understand electrochemical materials and phenomena at the atomic and molecular scale, and to use this fundamental knowledge to discover and design next generation energy storage technologies. (http://science.energy.gov/~media/bes/pdf/hubs/JCESR_Fact_Sheet.pdf)

2012) To analyze their performance capabilities, a Ragone plot (which plots power density against energy density on a logarithmic scale) is provided in Figure 1.2 to compare the performance of various energy storage technologies relative to the internal combustion engine (IC). (Wachsman & Lee 2011) Various goals for electric vehicles are labeled: EV, Hybrid EV, and Plug-in Hybrid EV. The *energy density* (Wh l^{-1}) is the amount of energy stored per unit volume of the battery, while the *power density* (W l^{-1}) is the amount of power per unit volume. Two other terms, *specific power* (W kg^{-1}) and *specific energy* (W h kg^{-1}) describe these properties as a function of the mass of the battery. By using the EV as an example, a higher energy density means that the car can be driven more miles before recharging the battery, while a higher power density means being able to accelerate more quickly from 0 to 60 mph.

A battery engineer will design batteries with variable battery performance for different applications. These applications can vary from a cell phone to an electric vehicle. The cell phone requires a battery with low power that lasts for as long as possible. However, if this same battery were placed in an electric vehicle, it would last for only a few seconds, because an electric vehicle requires a battery with a much higher power density. In practice, power and energy are two fundamental concepts of a battery that tend to work against each other.

The diagonal dotted lines from the lower left hand corner of the Ragone plot distinguish between the time it takes to charge or discharge these energy storage technologies (Figure 1.2). On one extreme, in the lower right-hand corner, a capacitor can be charged and discharged in less than one minute. (Wachsman & Lee 2011)

On the other extreme, some lithium ion batteries are charged in over 100 hours. Any energy storage technology that will be feasible in current portable energy systems needs to charge in under a few hours.(Chu 2007) This constraint limits the available technologies to supercapacitors, solid oxide fuel cells (SOFC), and batteries. The advantages and disadvantages of these three technologies will be discussed in the following section.

1.3 Supercapacitors, Solid Oxide Fuel cells, and Batteries

In supercapacitors, electrostatic energy is stored on the surface of the electrode interface. This electrostatic energy storage mechanism requires no chemical reactions and is known to provide relatively long cycle life compared to batteries. A supercapacitor may have high power,

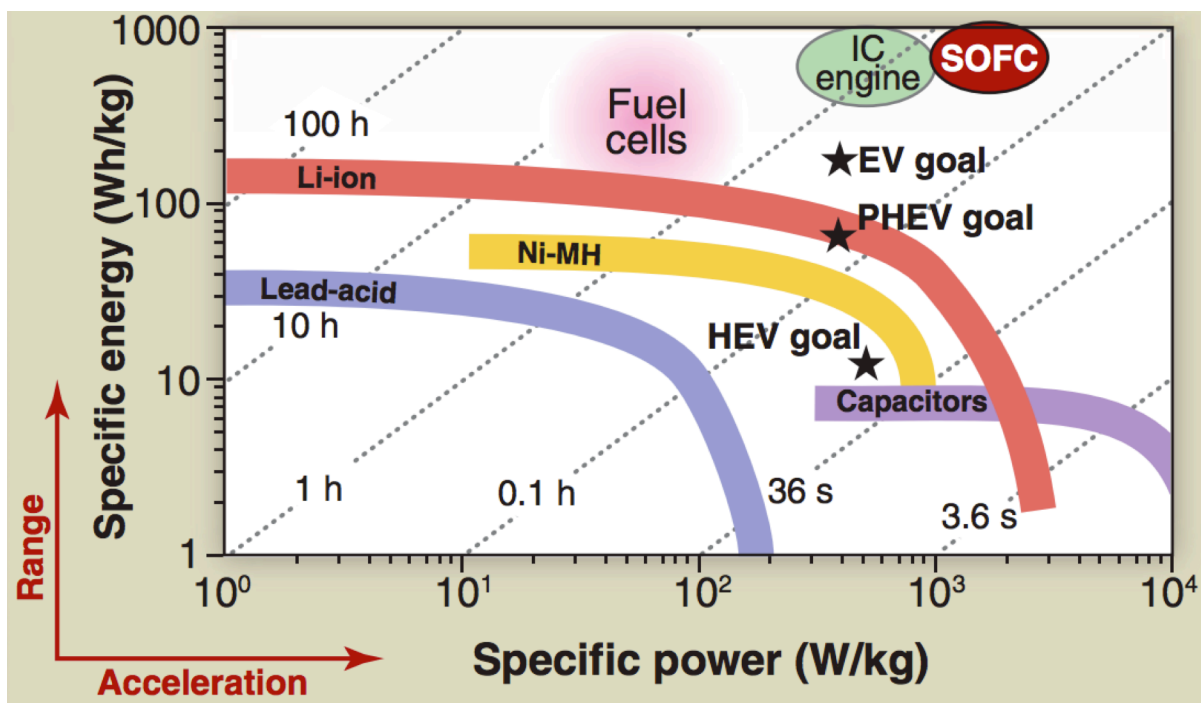


Figure 1.2 Ragone Plot depicting specific energy against specific power for various energy storage technologies. The diagonal lines represent the time of charge for each energy storage technology. (Wachsman & Lee 2011)

but the energy storage capacity is relatively limited compared to batteries; large supercapacitors have a specific energy density in the range of only $1 - 10 \text{ W h kg}^{-1}$. This is small compared to batteries, which can have specific energy densities between $25 - 150 \text{ W h kg}^{-1}$.(Chu 2007) Also, supercapacitors have an electrolyte between electrodes that can provide either high ionic conductivity with low break down voltages, or low ionic conductivity (high resistivity) with high breakdown voltage (ref). For example, aqueous liquid electrolytes such as sulfuric acid (H_2SO_4) and potassium hydroxide (KOH) have high ionic conductivities, but they limit the operational voltage due to their low breakdown potential of 1.2 V.(Chu 2007) Non-aqueous liquid electrolytes such as propylene carbonate and acetonitrile (CH_3CN) with dissolved salts provide a higher break down voltage with a resistance that is least an order of magnitude greater than aqueous electrolytes.(Chu 2007) Implementing this technology into EVs could be realized by integrating supercapacitors in addition to another energy storage technology that is capable of higher energy density for longer driving ranges(Burke & Miller 2011).

Fuel cells are not energy “storage” devices in the same way that capacitors and batteries are, in that fuel cells require an input flow of fuel to operate, and it produces an exhaust product: thus they are not chemically closed-cycle processes. We can still compare the performance of these devices within the context of energy storage, the same way that we can include comparisons with other chemically open processes like conventional combustion engines, where the energy is stored in a fuel tank. Fuel cells aim to achieve two general objectives: first, reducing CO_2 emissions, and second, contributing to the energy grid. A major benefit of fuel cells is that they typically have a high power density without a liquid electrolyte. A fuel cell that runs continuously on a supply of hydrogen gas and conducts oxygen ions is called a solid oxide

fuel cell (SOFC). SOFCs are a clean power source that has the benefit of producing water as a by-product through the consumption of various hydrocarbon fuels. The ionic transport properties of the SOFC electrolyte ultimately determine the energy density of the fuel cell. Problematic interfacial adherence and grain boundaries within the electrolyte are the predominant resistances of the entire cell. To overcome these resistances, the operating temperature of a SOFC is often above 800°C. This high operating temperature is a major cause for accelerated material degradation due to sintering of electrodes and interfacial reactions. Similarly, the choice of materials and fabrication methods are limited, adding to the cost of SOFCs. Due to these constraints, the SOFC may be integrated into an EV only if the temperature of the engine climbs into this high temperature range.

Energy storage technology goals need to be achieved for electric vehicles (EV goal in Figure 1) to replace internal combustion engines to power automobiles. Batteries could be the best suited for this, due to the low energy density of super capacitors and the high operating temperatures required for SOFCs. To date, however, only the nickel metal hydride and lithium ion batteries are capable of meeting plug-in hybrid electric requirements (Budde-Meiwes *et al.* 2013).

This perspective outlines the main motivation for the present study, which is focused on understanding and improving Li-ion batteries. The following introductory sections will outline the basic function of a battery, describe the state of the art in lithium ion battery technologies (including their many advantages and disadvantages), and identify avenues through which lithium-ion batteries may be improved.

1.4 The battery: schematic and operating mechanism

The history of batteries started with the observation of charge transfer between two electrically conducting mediums. As stated by Haas (1993),

“[Luigi] Galvani (1775 – 1836) observed that static electricity that was stored in a Leyden jar² caused dissected frogs' legs to twitch. This occurred if they were placed on metal during a thunderstorm.”

This early example of electrical energy transfer spurred further research on the transfer of electricity, ultimately leading to the development of the battery. Luigi Galvani may not have come to the right conclusion—he believed that the source of electricity was in the nerves and muscles of the animal—but he did, however, set the stage for other scientists to develop the concept of transferring electricity through a conducting circuit. By 1793, Alessandro Volta had disproved Galvani's findings by implementing the Crown of Cups experiments.(Volta 1800) He went on to invent the first electric battery, in the form of copper and zinc plates immersed in “acidulated water” in 1800.(Jones 1911) Volta was also one of the first scientists to establish the principle of converting chemical energy to electrical energy using spontaneous redox reactions at two electrodes. Once this principle was established, battery research progressed to primary batteries, based on irreversible redox reactions that are able to discharge energy only once, and rechargeable batteries, which can reversibly charge and discharge over many cycles.

Every battery has three basic components: a positive electrode, a negative electrode, and an electrolyte between them (Figure 1.3). The electrodes are separated by the electrolyte but

² One of the first capacitors developed simultaneously by German cleric E. Georg von Kleist and Dutch physicist Pieter van Musschenbroek in 1745. Benjamin Franklin is famous for his 1752 experiment to collect the charge from a storm cloud into a Leyden jar with a key attached to a kite. (www.magnet.fsu.edu)

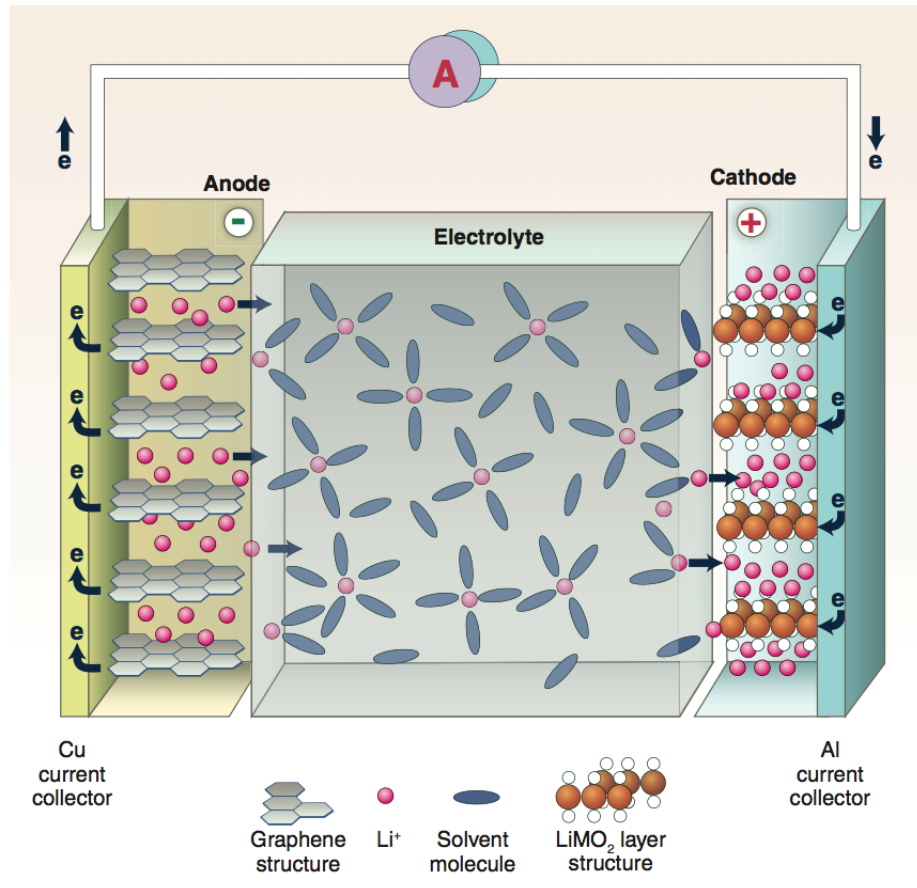


Figure 1.3 Schematic of a lithium ion battery (LIB) (Dunn et al. 2011)

connected through an external circuit, through which an electric current can flow. The electrolyte acts like a filter by blocking the flow of electrons and instead allowing only ions to pass through. When these components are connected in a circuit, the electrode that is more negatively charged will provide a source of electrons that can move through the circuit toward the positive electrode (Figure 1.3). An ionic current will simultaneously travel through the electrolyte to spontaneously decrease the potential difference caused by the flow of electrons.

In the following section, various battery chemistries, their advantages and disadvantages, and the feasibility of using them as the energy storage device in an EV will be discussed.

1.5 State of the art batteries

‘The system of electricity will be the system of chemistry and vice versa’

- Wilhelm Ritter (1776 – 1859) (Kurzweil 2009)

Now that the battery components have been discussed, it is necessary to describe the industrial products that are used in current ICE vehicles and EVs. Automobiles have been continuously improved upon to run farther and faster on a single tank of gas. This is partially a result of the size of the gas tank, the number of cylinders in the engine, and the properties of the battery. Since cost is a major consideration for purchasing cars, it is desirable for each component in an automobile to be lightweight, durable, and inexpensive. In spite of various wide-scale improvements in battery technologies over the last 200 years, Lead-Acid (LA) batteries have remained the standard for automobiles, mostly due to the lack of a suitable replacement.(Kurzweil 2009) This is true because the parts are cheap and nearly 95% recyclable(Budde-Meiwes *et al.* 2013). These advantages of LA batteries persist even when weighed against the corresponding disadvantages, such as the weight of lead, the toxicity of components, and the initial charging time of nearly 14 h.

Nickel-Cadmium battery research began in 1899 by Ernst Waldemar Jungner with a cadmium negative electrode, nickel positive electrode, and nonwoven fabric separator in potassium hydroxide electrolyte.(Kurzweil 2009) This battery is more costly than the lead-acid battery because of the materials, but it has a higher energy density and significantly higher power density. This battery will probably not be manufactured in the future due to the environmental concerns related to cadmium uptake into the soil. Cadmium is so toxic that this metal has already been banned in the European Union and has not been put into circulation by manufacturers of electric equipment since 2006.(Kurzweil 2009)

To address the environmental issues with the Ni-Cd battery, gaseous hydrogen in titanium-based alloys has been used in place of cadmium as the negative electrode.(Kurzweil 2009) This battery technology, known as the Nickel-metal hydride (NMH) battery, became one of the most promising battery technologies for portable energy storage in the early 1990s due to energy densities of 50-80 Wh kg⁻¹. (Kurzweil 2009) The variety of cell designs—button, round, or prismatic cells—also demonstrated the versatility of this battery type for cellular phones, computers, and hybrid EVs.(Budde-Meiwes *et al.* 2013) The NMH battery has nearly identical cell voltages, discharge curves, and charge curves to that of the Ni-Cd battery (Budde-Meiwes 2013). NMH batteries still have drawbacks related to operating temperatures and the batteries' memory effect, however, which hinders their suitability for long-term use in portable energy storage technologies. Car manufacturers like Toyota, Honda, and Lexus currently use Ni-Metal Hydride batteries in hybrid vehicles because the energy density is twice that of Ni-Cd, and because the power density is close to 1000 W kg⁻¹. (Budde-Meiwes *et al.* 2013)

To further increase the specific energy of rechargeable batteries, researchers have begun investigating lithium batteries due to the intrinsic properties of elemental lithium as the most electropositive metal (-3.04 V versus a standard hydrogen electrode) (Tarascon & Armand 2001) Initially, the development of the lithium battery was hampered due to issues related to the inherent instability of lithium anodes in primary cells(Kurzweil 2009). However, once it was discovered that lithium forms an intercalation compound in a layered grid of carbon or graphite (Li_xC₆), the true potential of a high-energy rechargeable Li system was realized.(Kurzweil 2009) Further work by John B Goodenough on lithium cobalt and lithium manganese spinels as cathodic materials enabled the full development of lithium-based rechargeable battery

systems.(Kurzweil 2009) The first Li ion batteries were produced by Sony cooperation in 1991 with a potential of approximately 3.6 V, specific energy densities between 120—150 W h kg⁻¹ (Tarascon & Armand 2001), and a specific power density of 1000 W kg⁻¹.(Chu 2007)

Researchers are still investigating rechargeable lithium ion battery (LIB) systems with metallic lithium as the negative electrode. Continued issues at the metallic lithium/liquid electrolyte interface, such as the growth of lithium dendrites on the surface of the anode after many charge/discharge cycles, still hinder further development. Lithium dendrites tend to grow through the electrolyte/separator and cause a short circuit when one reaches the cathode. Once it forms, this short circuit immediately releases its energy. In turn, the electrolyte surrounding the dendrite vaporizes and causes the internal pressure of the battery to rise, which can lead to explosions.

The US DoE lists the main challenges to the further development of LIBs as:

- 1) high production cost and lack of scalability;
- 2) extreme sensitivity to over-temperature, over-charge and internal pressure buildup;
- 3) intolerance to deep discharges due to irreversible phase change effects.(Chu 2007)

Of these concerns, three specific issues—the production cost, over temperature sensitivity, and internal pressure buildup—are related to minimizing the hazards associated with liquid electrolytes inside LIBs. It is therefore prudent to investigate alternative electrolytes that will inhibit dendrite penetration while still maintaining high ionic conductivity.

Another reason to investigate alternative electrolytes is to develop systems beyond Li-ion technology.(Bruce *et al.* 2011) Optimizing beyond Li-ion battery systems will provide EVs with the specific energy and energy density required for longer travel distances between recharging

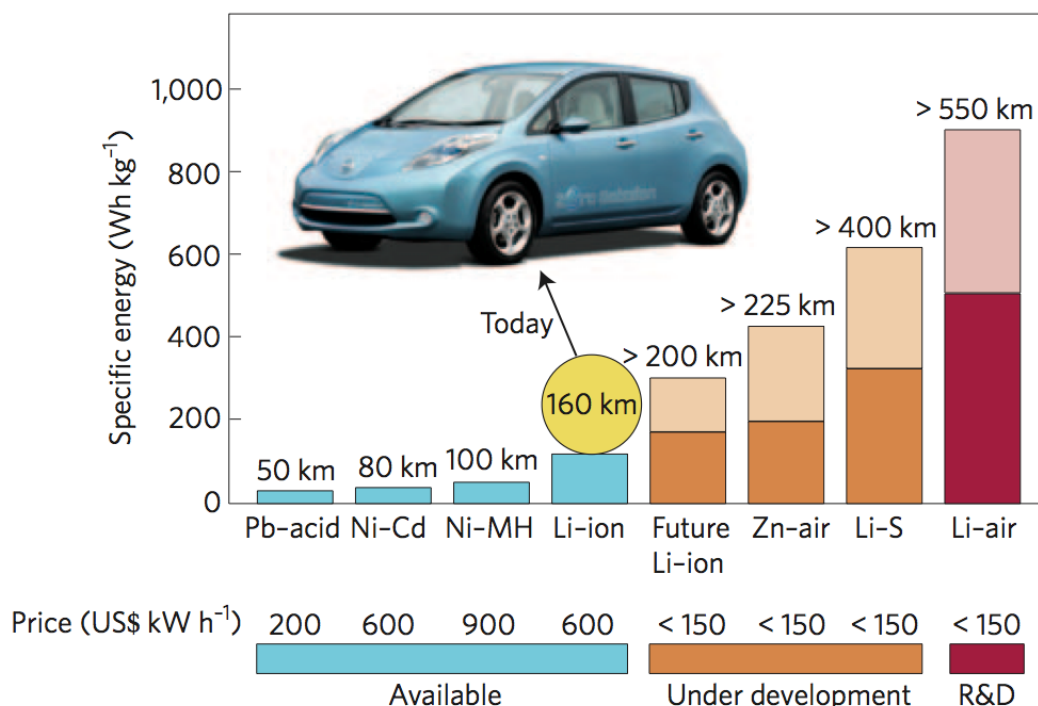


Figure 1.4 Comparison of current and potential battery technologies with their specific energies (Wh kg⁻¹) and prices (US\$ kWh⁻¹) listed. The blue bars indicate current batteries available for hybrid electric vehicles. The bars with lighter portions indicate the specific energies for potential battery chemistries under development with the driving ranges displayed above each bar. (Bruce et al. 2011)

(Figure 3). (Bruce *et al.* 2011) To extend the driving distance of an EV over 300 miles per charge, a cell-level specific energy of 350–400 Wh kg⁻¹ is necessary. (Song *et al.* 2013) Two examples of beyond Li-ion battery systems that have theoretical specific energies greater than 400 Wh kg⁻¹ are the metal-air (Li-O₂) and lithium-sulfur (Li-S) systems. (Bruce *et al.* 2011)

To attain the needed specific energy, metallic lithium would still be used as the anode but the cathodic material could be atmospheric oxygen or a mix of elemental sulfur (S₈ rings) with carbon, respectively. (Budde-Meiwes *et al.* 2013) The energy density is higher in the Li-O₂

system because the active mass is that of the metallic Li and the electrolyte; upon discharge, however, the energy density actually decreases due to the formation of a metal oxide on the anode.(Budde-Meiwes *et al.* 2013) A Li-O₂ system has a theoretical energy density between 2-3 kWh l⁻¹ based on the sum of the volumes of Li at the beginning and Li₂O₂ at the end of discharge, and depending on the type of liquid electrolyte (aqueous or non-aqueous). (Bruce *et al.* 2011) This theoretical energy density is based on aqueous and non-aqueous electrolytes that provide high ionic conductivity but few other advantages, such as chemical stability, temperature range, or structural support. Some major concerns about the O₂ cathode are related to O₂ and/or H₂O contamination of the electrolyte.(Bruce *et al.* 2011) Any contamination of the electrolyte could lead to its degradation and thus reduce the battery's cycle life. An ion selective membrane or an electrolyte that is stable against O₂ and H₂O would be required to prevent this contamination.

The Li-S system is a promising candidate because of the high theoretical specific energy of ~ 2600 Wh kg⁻¹ as well as the natural abundance and low cost of sulfur.(Bruce *et al.* 2011; Song *et al.* 2013) The large predicted specific energy is due to the very high specific capacity of elemental sulfur (1675 mAh g⁻¹) based on the two electron reaction ($S + 2Li^+ + 2e^- \leftrightarrow Li_2S$). In the Li-S system, the reaction occurs between lithium and sulfur to form polysulfides such as the intermediate Li₂S_x species (3 < x < 6).(Song *et al.* 2013; Bruce *et al.* 2011) A chemical degradation mechanism has been reported where soluble polysulfides shuttle from the cathode and reduce to insoluble Li₂S₂ and/or Li₂S on the metallic lithium anode surface.(Budde-Meiwes

et al. 2013; Song *et al.* 2013) Another degradation mechanism related to the conversion reaction between S and Li_2S involves a $\sim 76\%$ volume expansion/contraction during cycling, which leads to premature electrode failure.(Song *et al.* 2013) Song *et al* have addressed both degradation mechanisms by using graphene oxide-sulfur (S-GO) nanocomposites to significantly improve the cycle life of the Li-S system. Their work revealed that the outer layer of sulfur must be protected from dissolving, while the inner layer of sulfur can be immobilized by the functional groups on the GO. There are still challenges associated with this system that arise from the cost of packaging both a liquid/gel electrolyte. The use of air-stable solid electrolytes could eliminate this problem.

The following section will focus on the general concept of solid ceramics as alternative electrolyte state-of-the-art liquid electrolytes used in LIBs. The necessary performance criteria will be discussed, including a focus on some specific promising ceramic electrolyte systems that will describe their advantages, disadvantages, and applicability to EVs.

1.6 Inorganic superionic conducting oxide (SCO) electrolytes

Superionic conducting oxide (SCO) electrolytes are inorganic, non-metallic ceramic compounds. that generally exhibit relatively high hardness, high compressive strength, and chemical inertness compared to sulfide or polymer electrolytes, thus making them appealing for solid-state batteries. Inorganic SCO electrolytes can be classified into two crystallographic categories: crystalline and amorphous. Extensive reviews of various SCO electrolytes have been reported elsewhere.(Roberston *et al.* 1997; Knauth 2009) A short review of several SCO electrolytes will be discussed in the following section.

1.6.1 Necessary SCO electrolyte performance criteria

According to Goodenough *et al.*, a practical solid-electrolyte membrane needs (Goodenough & Park 2013):

(a) $\sigma_{\text{Li}} > 10^{-4} \text{ S cm}^{-1}$;

(b) the capability to block Li dendrites;

(c) to be chemically and electrochemically stable; and

(d) to be easily fabricated into a mechanically robust, flexible thin (<100 μm) membranes

These SCO electrolyte performance criteria are basic requirements that could enable beyond Li-ion technologies. To this end, the SCO electrolyte requirements are only a guide to improve the solid-state battery technology to minimize electrolyte degradation for a long cycle life, enable facile large-scale manufacturing, and to attain the needed specific energies for increased EV driving ranges.

1.6.2 Review of SCO electrolytes

1. Perovskite type Li ion conductors

LLTO ($\text{Li}_{3x}\text{La}_{(2/3)-x}\text{Ti}_{(1/3)-2x}\text{TiO}_3$) [$0 < x < 0.16$]

The Perovskite-type structure, with the general formula ABX_3 , has a three dimensional crystal structure composed of corner sharing BX_6 octahedra that make up the skeleton of this structure. Within the skeleton structure, Li^+ ions are distributed in a network of occupied and unoccupied A-sites. The highest ionic conductivity reported in such materials for lithium ion battery applications was achieved through Li^+ A-site substitutions in lanthanum lithium titanate ($\text{La}_{2/3-x}\text{Li}_x(\text{TiO}_3)$) (LLTO) with $x \sim 0.11$, which resulted in a total conductivity of $5.25 \times 10^{-5} \text{ S}$

cm^{-1} .(Inaguma *et al.* 1994; Teng *et al.* 2014) Ionic transport in the Perovskite structure is mainly attributed to conduction through A-site vacancy channels. These vacancies allow Li^+ ions to jump to adjacent sites through a planar bottleneck formed by four neighboring oxygen ions(Teng *et al.* 2014), and the mobility of the ions is directly affected by the size of this bottleneck.(Knauth 2009) This parameter is dependent on the lattice parameter as well as structural distortions, which can manifest (for example) as a slight tilt into the octahedral-type unit cell.(Inaguma *et al.* 1994)

As discussed above, one of the greatest advantages to the Perovskite structure is the high ionic conductivity of $\sim 10^{-3} \text{ S cm}^{-1}$ at room temperature (RT) for a single crystal.(Knauth 2009) This SCO electrolyte has a total ionic conductivity of $10^{-5} \text{ S cm}^{-1}$ in bulk polycrystalline LLTO, which is about two orders of magnitude lower than what has been observed in a single crystal. This difference has been attributed to limiting effects of slow ionic conduction through grain boundaries in the bulk polycrystalline material.(Knauth 2009) Also, this structure will not be applicable for high energy density lithium ion battery applications because it is not stable against metallic lithium: the titanium cation spontaneously reduces from Ti^{4+} to Ti^{3+} .

2. NASICON-type ion conductor

LATP ($\text{Li}_{1.3}\text{Al}_{0.3}\text{Ti}_{1.7}(\text{PO}_4)_3$)

The *NA*-ion Superior Ionic *CON*ductor-type (NASICON) solid ion conductor has the general formula $[\text{A}_2\text{P}_3\text{O}_{12}]^-$ with AO_6 octahedra connected to PO_4 tetrahedra by sharing an oxygen atom at their corners. The crystal structure forms a 3D connected network with two interstitial sites in between the corner-sharing octahedra and tetrahedra. In this structure, conductor cations

in the interstitial sites move from one site to the next by jumping through bottlenecks between the polyhedron.(Knauth 2009) One advantage to this structure is that it can reversibly cycle various cations (Na^+ , Li^+ , Ag^+ , K^+). (Knauth 2009) One of the first SCO electrolytes with a NASICON structure was $\text{NaM}_2^{\text{IV}}(\text{PO}_4)_3$ with common dopants ($\text{M}^{\text{IV}} = \text{Ge}, \text{Ti}, \text{and Zr}$), which was first identified in 1968.(Hagman & Kierkegaard 1968) Originally, this structure was designed with Na cations on the interstitial sites, as the name of the structure suggests.(Hagman & Kierkegaard 1968) Since then, researchers have replaced Na with Li, which has resulted in Li^+ ionic conductivity of $\sim 10^{-3} \text{ S cm}^{-1}$ at RT in this compound.(Knauth 2009) Aono *et al* reported the highest ionic conductivity in the NASICON structure in the LATP ($\text{Li}_{1.3}\text{Al}_{0.3}\text{Ti}_{1.7}(\text{PO}_4)_3$) system, which has a bulk Li^+ ionic conductivity of $3 \times 10^{-3} \text{ S cm}^{-1}$ at RT.(Aono 1990)

In addition to these advantages inherent to the NASICON structure, there are also several disadvantages. Gellert *et al* have found that grain boundary effects are important due to the formation of highly defective layers with a thickness range of 5 – 10 nm at the grain boundaries.(Gellert *et al.* 2012) These defective layers behave as scattering sites for ion transportation that increase the effective activation energy and reduce the ionic conductivity from $10^{-3} \text{ S cm}^{-1}$ to $10^{-5} \text{ S cm}^{-1}$.(Teng *et al.* 2014; Gellert *et al.* 2012) Another disadvantage is similar to the major concern with the Perovskite-type SCO electrolyte: the highest ionic conductivity in NASICON structures was reported in Ti-based materials, where the reduction of Ti^{4+} to Ti^{3+} again causes a significant change in the internal structure.

3. LISICON and thio-LISICON

The Li superionic Conductor (LISICON) structure, $\text{Li}_{14}\text{Zn}(\text{GeO}_4)_4$, was first investigated by Hong *et al* in 1978. They reported that using this three dimensional structure of LiO_4 and GeO_4 tetrahedra, in which the O^{-2} ions are bonded to four network cations, deflected the oxygen charge density away from the Li^+ ions.(Hong 1978) Hong *et al* also reported that this structure is closely related to the high-temperature lithium orthophosphate phase $\gamma\text{-Li}_3\text{PO}_4$, and that $\text{Li}_{14}\text{Zn}(\text{GeO}_4)_4$ had the highest conductivity of any Li^+ ion conductor (0.13 S cm^{-1} at 300°C).(Hong 1978)

The LISICON structure is comprised of corner-sharing tetrahedron and contains two interstitial sites occupied by Li^+ ions in the range $-0.36 < x < +0.87$ for $\text{Li}_{2+2x}\text{Zn}_{1-x}\text{GeO}_4$.(Roberston *et al.* 1997) These occupied interstitial sites are the basis for ionic conduction within this system. At low temperatures, however, the lithium ions tend to become immobile along this sublattice.(Roberston *et al.* 1997) Several disadvantages of using $\text{Li}_{14}\text{Zn}(\text{GeO}_4)_4$ as a SCO electrolyte are the low ionic conductivity of $10^{-6} \text{ S cm}^{-1}$ at RT, high reactivity against metallic lithium and with CO_2 exposure, and degradation of the material performance after several charging cycles.(Roberston *et al.* 1997; Knauth 2009)

To address the low temperature Li^+ trapping issues with the LISICON structure, Kanno *et al* developed Thio-LISICON. This material is different in that the oxide ions are replaced with sulfide ions, which are larger and more polarizable.(Kanno *et al.* 2000; Knauth 2009) This

modification makes it possible to dope the material with a wide range of aliovalent elements, and electrochemical tests indicate that this structure is stable up to 5 V against metallic lithium.(Kanno *et al.* 2000) The lithium ion conductivity in the thio-LISICON structure has also been investigated, and an enhancement of the total lithium ion conductivity up to $6.5 \times 10^{-5} \text{ S cm}^{-1}$ has been observed. This increase has been attributed to the larger bottleneck size and greater polarizability of the sulfide ions compared to the oxygen ions. (Kanno *et al.* 2000)

4. LiPON,

Lithium phosphorous oxy-nitride (LiPON) is a thin film SCO electrolyte that has a moderate Li^+ ion conductivity of $10^{-6} \text{ S cm}^{-1}$ and is stable against a metallic lithium anode. Initial investigation of radio frequency (RF)-magnetron sputtering of Li_3PO_4 in N_2 resulted in $1\mu\text{m}$ films that exhibited an amorphous structure and reasonably high ionic mobility of $2.2 \times 10^{-6} \text{ S cm}^{-1}$, as observed by Bates *et al* at RT in a $\text{Li}_{3.3}\text{PO}_{3.0}\text{N}_{0.17}$ sample produced by sputtering in a pure N_2 environment.(Bate *et al.* 2002) Though this material exhibits excellent resistance against water and salt corrosion, this system is capable of high ionic conductivity in only its thin film form,(Bate *et al.* 2002) which makes it better suited for micro lithium ion batteries.(Yu *et al.* 1997) It is also a viable candidate for coating other solid electrolytes such as LATP because it prevents the reduction of Ti^{4+} to Ti^{3+} .

5. Garnet-type LiLaZrO electrolytes

The garnet-type Li^+ ion conductor is stable against metallic Li and exhibits a conductivity of $\sim 10^{-4} \text{ S cm}^{-1}$. This particular metal oxide group has a nominal composition of $\text{Li}_2\text{La}_2\text{M}_3\text{O}_{12}$ (M = Nb, Ta, Zr) and was first reported by Murugan *et al* to have high Li^+ ionic conduction around $10^{-4} \text{ S cm}^{-1}$. (Murugan *et al.* 2007) Like the spinel $[\text{B}_2]\text{O}_4$ structure, the garnet structure contains an interstitial space consisting of tetrahedral A sites bridged by face-sharing octahedral sites with two A sites on opposite sides. (Goodenough & Park 2013) The garnet structure can accommodate cations of different valence states and sizes without a significant change in the symmetry. (Murugan *et al.* 2007) The combination of high lithium ion conductivity, good thermal and chemical stability, low environmental impact, low cost, and ease of preparation of $\text{Li}_7\text{La}_3\text{Zr}_2\text{O}_{12}$ together suggest that this material is a promising SCO electrolyte for all-solid-state Li-ion batteries. (Murugan *et al.* 2007)

Going beyond Li-ion requires suitable electrolytes must be developed that have an ionic conductivity greater than $10^{-4} \text{ S cm}^{-1}$ and are stable against the metallic lithium electrode and either oxygen or sulfur electrodes on the other. Several SCO electrolytes, such as the Perovskite- and NASICON-based structures discussed in the previous section, have already demonstrated ionic conductivity values in this range. However, these SCOs also reduce against metallic Li and are therefore unable to meet the overall requirements needed for a beyond Li-ion technologies. To improve the cycling capabilities, LIPON has also been discussed as a promising candidate, but this system is practical only as a thin film membrane. Unfortunately, even as a thin film SCO electrolyte (which means low capacity) the LIPON compound has attained ionic conductivity values on the order of only $10^{-6} \text{ S cm}^{-1}$, which excludes this electrolyte as a candidate for EV

applications. Finally, the family of Garnet-type SCO electrolyte compounds has drawn significant attention for their stability against electrode materials and high ionic conductivity ($\sim 10^{-4}$ S cm⁻¹). These compounds are the only family identified so far that meet the required specifications for beyond Li-ion technologies.

The problem with current SCO electrolytes for beyond Li-ion technology, as with any liquid electrolyte system, is that metallic lithium has been reported to form lithium dendrites after many charging cycles. (Ishiguro *et al.* 2013) As was discussed earlier, the formation of Li dendrites poses a safety hazard and is detrimental to the life of a battery. It has been proposed that using SCO electrolytes will prevent the penetration of dendrites through the electrolyte, although this has not been confirmed. Monroe *et al* report that an electrolyte must have > 8 GPa shear modulus to prevent the penetration of dendrites. (Monroe & Newman 2005) This also implies the electrolyte must have high relative density and at the minimum does not have interconnected porosity. The solution is to develop practical material processing techniques focused on improving the density.

This study proposes an SCO electrolyte as a candidate for the solid electrolyte in a lithium ion battery (LIB) as a possible solution for addressing the technological issues outlined above. More specifically, this study investigates the processing methods of the Li-based solid electrolyte Li₇La₃Zr₂Al_{0.24}O₁₂ (LLZO) and how varying the densification conditions (Chapter 2) and adding sintering aids (Chapter 3) affects both the microstructure and ionic conductivity.

1.7 Ceramic processing techniques

All ceramists have an ultimate goal that pertains to their work in research:

“if there were such a thing as the holy grail of ceramic processing science, it probably would

be how consistently to obtain theoretical density [of a ceramic body] at the lowest possible temperature.” –Barsoum(Barsoum 2002)

To achieve the highest densities, the principal considerations are extremely small particle size starting material and the temperature at which the ceramic powder transforms to a strong, dense ceramic body upon heating.(Kingery 1963) Since ceramic materials typically have high melting temperatures, care is taken to process the ceramic powder so that atomic processes leading to densification dominate over the processes that lead to coarsening, which is detrimental to the properties of the bulk ceramic. The processing method to fuse particles is called firing, or *sintering*. Densification of ceramic powder is achieved when sintering fuses the particle and eliminates internal porosity, thereby causing the ceramic body to shrink. The majority of ceramic materials have been processed to near theoretical densities by solid-state sintering or liquid-phase sintering.(Fang 2010) In liquid-phase sintering, the sintering temperature and ceramic powder composition (the ratio of ceramic powder to additions of a sintering aid) are chosen such that some liquid is formed during processing.(Barsoum 2002; Fang 2010) Solid-state sintering occurs in the absence of a liquid additive and relies on solid-state diffusion of mass and vacancy diffusion to remove porosity during the final stage of sintering. Along with the temperature at which the ceramic powder is sintered, other variables such as sintering time and initial particle size determine the rate at which densification occurs.(Kingery 1960; Barsoum 2002; Fang 2010)

In the present study, time and particle size have been held constant while temperature and the amount of a sintering aid were varied. Solid-state sintering of the SCO electrolyte LLZO was investigated by changing the temperature at which this material was densified under constant pressure and liquid-phase sintering was investigated by adding varying amounts of an additive to LLZO powder under constant pressure. The results of these investigations will be

covered in Chapters 2 and 3, while the next two sections will provide a review of solid state sintering via hot pressing compared to pressure-less sintering and liquid phase sintering.

1.7.1 Comparison of hot pressing and pressure-less sintering methods

High-density SCO electrolytes are necessary to attain low resistance to ion conduction and improve strength. These characteristics increase the performance and could ease the manufacturing of solid-state batteries.(Virkar *et al.* 1979) Microstructural properties of a sintered ceramic body inherently affect the macroscopic electrical properties. Significant efforts have been taken to investigate the factors that influence the microstructural properties, such as grain size distribution, grain boundary characteristics, and porosity.(Fang 2010) The ultimate goal of attaining a high density SCO electrolyte can be achieved by minimizing porosity through optimized sintering conditions with respect to time, temperature, and chemical compositions.(Fang 2010)

Solid state sintering of cold-pressed powder LLZO pellets has been previously investigated and several techniques have been used to achieve high relative densities above 90%.(Huang *et al.* 2011; Awaka *et al.* 2011; Jin & McGinn 2011; Murugan *et al.* 2007) A brief review of two such techniques, pressure-less sintering and hot pressing, will be covered in the following section.

Pressure-less sintering of LLZO has been reported to densify LLZO. For this procedure, it is common to heat a cold-pressed LLZO pellet to high temperatures (900 – 1230°C) covered by and set on a substrate of LLZO powder to prevent lithium loss at high sintering temperatures and unintentional doping due to the substrate material, respectively.(Rangasamy *et al.* 2012) Recent work has been done to explore the efficacy of pressure-less sintering, but these results indicate that sintering times of approximately 36 h are necessary to get densities near

95%.(Huang *et al.* 2011; Murugan *et al.* 2007; Yutao Li *et al.* 2012) A comparison of these results to previous work on hot pressed samples indicate that hot pressing ceramic powder can achieve similar densities in a much shorter time. For example, two studies of solid ceramic systems other than LLZO have used uniaxial hot pressing and observed comparable results: Virkar *et al* have reported that hot pressing in a vacuum atmosphere significantly increased the density of Na- β Alumina solid electrolyte at a lower temperature than conventional sintering methods,(Virkar *et al.* 1979) and Naziripour *et al* have reported high quality hot pressed Yttrium iron garnet via uniaxial hot pressing, which enabled microstructural control *vis-a-vis* porosity and grain size by varying sintering temperature and pressure.(Naziripour *et al.* 1985) A third report of hot pressing that attained a relative density of 98%, in only 1 h is the garnet-based LLZO system. (Rangasamy *et al.* 2012) This is a large milestone in sintering any ceramic to near theoretical density in such a short time.

All of these examples indicate that hot pressing is a technique capable of producing high-density ceramic pellets. Currently, only the ionic conductivity of LLZO related to varying dopants has been investigated.(Thangadurai *et al.* 2003; Allen *et al.* 2012) To examine the efficacy of this technique for microstructural control, it is necessary to study the role of sintering temperature and correlated grain boundary effects on the ionic conductivity of hot pressed LLZO. This subject has been investigated in this study, and will be further discussed in Chapter 2.

1.7.2 Sintering aids for Liquid-Phase Sintering

Another method to increase the density of structural ceramics is called liquid phase sintering (LPS) and requires mixing small amounts (on the order of a few volume percent or less) of low melting temperature sintering aids to the ceramic powder to be sintered.(German *et al.*

2008) This method is different than relying on sintering via pressure-less or hot pressing alone because it requires understanding the chemistry between the sintering aid and the matrix material. LPS is more sensitive to processing variables than other forms of sintering. Therefore, it is necessary to understand the physical properties such as melting temperature, phase transition temperature, and decomposition temperatures of the matrix material, the sintering aid, and the two combined.

There are three stages of liquid phase sintering that are important to densification. Kingery, *et al.* state that, “rapid densification is obtained first by rearrangement of the solid particles under the forces of capillary action by sliding over one another with little friction between them, and second by solution at the contact point and precipitation elsewhere”.(Kingery 1963) Fang, *et al.* comment in detail about the solid material dissolving into solution, from which the “material located at convex particle surfaces starts to dissolve and can now migrate to pore surfaces where it precipitates out of solution to lower the system free energy.”(Fang 2010) This stage, called solution-precipitation, is only possible in LPS. Individual grains commonly change shape during this stage because the porosity between the grains is filled with precipitated material after diffusing through the liquid phase. The final stage of LPS, similar to solid-state sintering occurs when closed porosity is formed, and is generally characterized by the shrinkage of isolated pores and grain growth.(Fang 2010)

The following chapters will focus on two studies conducted on the SCO electrolyte LLZO. The salient properties of this material, after high temperature processing will be discussed, including a focus on the effects of altering sintering temperature and sintering additive.

2. Effect of hot pressing temperature on the microstructure and Li-ion transport of $\text{Li}_6\text{La}_3\text{Zr}_2\text{Al}_{0.34}\text{O}_{12}$

2.1 Introduction

Li-ion battery technology has advanced significantly in the last two decades (Tarascon & Armand 2001; Dunn *et al.* 2011; Bruce *et al.* 2011); however, future energy storage demands will require safer, cheaper and higher performance electrochemical energy storage (Bruce *et al.* 2011; Committee on Climate Change 2012). While the primary strategy for improving performance has focused on electrode materials, the development of new solid electrolytes has been overlooked as a potential means to revolutionize electrochemical energy storage. Examples of technologies could include: i) all-ceramic Li-ion batteries that are inherently stable and do not require hermetic packaging, ii) ambient temperature Li-S batteries, iii) molten alkali-S, and iv) redox flow batteries. Indeed the need for superionic Li-conducting ceramics is clear, but relatively few have been identified as promising candidates.

Recently, zirconia-based garnet electrolyte, with the formulation $\text{Li}_6\text{La}_3\text{Al}_{0.34}\text{Zr}_2\text{O}_{12}$ (LLZO), was reported to have the unique combination of high room temperature Li-ion conductivity, stability against metallic Li, and moderate stability in air (Goodenough 1984; Murugan *et al.* 2007; Ohta *et al.* 2011; Shimonishi *et al.* 2011; Rangasamy *et al.* 2012; Allen *et al.* 2012). Room temperature conductivities have been reported ranging from 0.4 to 0.9 mS cm^{-1} at room temperature (Goodenough & Kim 2010; Murugan *et al.* 2007; Ohta *et al.* 2011; Shimonishi *et al.* 2011; Rangasamy *et al.* 2012; Allen *et al.* 2012), which is comparable to state-of-the-art Li-ion membranes consisting of a porous polymer membrane permeated with liquid electrolyte (0.4 mS cm^{-1}). (Wong *et al.* 2012) Replacing a state-of-the-art Li-ion membranes with a ceramic membrane such as LLZO of comparable thickness ($\sim 40 \mu\text{m}$), however, is challenging

owing to the inherently brittle nature of ceramics. LLZO(Wolfenstine *et al.* 2012), like other ceramic oxide electrolytes(Wolfenstine *et al.* 2010; Wolfenstine *et al.* 2013; Jackman & Cutler 2012), have fracture toughness values in the $\sim 1 \text{ MPa m}^{-0.5}$, which is considered relatively brittle. Thus, the development of relatively thin LLZO membranes requires approaches to increase fracture toughness and flexural strength, while maintaining adequate ionic conductivity. A common approach involves controlling the microstructure; specifically, reducing porosity and grains size.(Barsoum 2002) However, while reducing the porosity will also improve ionic conductivity, decreasing the grain size increases grain boundary resistance thereby decreasing conductivity.(Ban & Choi 2001) Typically, grain boundaries impede ionic transport, thus larger grains are preferred to maximize conductivity. These countering effects of grain size suggest the grain size should be optimized to achieve adequate mechanical properties to prevent fracture, while maintaining sufficient ionic conductivity.

Ceramics components are often densified using pressure-less sintering where porosity decreases and the grain size increases with increasing temperature and time.(Barsoum 2002) Likewise, for the purpose of isolating and studying the effects of just grain size, it can be difficult to control the grain size while maintaining the same porosity. Here we used rapid induction hot pressing (RIHP) where the simultaneous application of heat and pressure reduces the densification temperature and time.(Virkar *et al.* 1979) Induction heating allowed for relatively rapid heating rates ($\sim 200^\circ\text{C min}^{-1}$) to reduce Li loss, which can also be a variable.(Ban & Choi 2001) We hot pressed LLZO between 900 and 1100°C at a fixed pressure (23 MPa) to determine how the hot pressing temperature affects the microstructure and ionic transport. We acknowledge that detailed mechanical properties should be conducted in

conjunction with the ionic conductivity characterization, but the number of samples required to establish statistical relevance (typically $n \geq 30$) goes beyond the current scope of this work.

2.2 Experimental Methods

2.2.1 Powder Preparation and Hot-Pressing Technique

Samples of $\text{Li}_6\text{La}_3\text{Zr}_2\text{Al}_{0.34}\text{O}_{12} + 10 \text{ wt}\% \text{Li}_2\text{CO}_3$ were prepared by solid-state reaction similar to that described by Rangasamy *et al.* (Rangasamy *et al.* 2012), Murugan *et al.* (Murugan *et al.* 2007) and Huang *et al.* (Huang *et al.* 2011). The raw materials of Li_2CO_3 (Alpha Aesar, Ward Hill, MA), $\text{La}(\text{OH})_3$ (Alpha Aesar), Al_2O_3 (Mager Scientific Inc, Dexter, MI), and ZrO_2 (Inframat® Advanced Materials, Manchester, CT) were weighed and combined in an agate vial according to the stoichiometric ratio. This powder mixture was dry-milled in a planetary mill for 4 h at 350 rpm, then pressed into pellets in a 1” stainless steel die, and calcined at 1000°C for 4 h. The final powder was obtained by grinding the calcined pellets with a mortar and pestle, reducing agglomeration by ball-milling, collecting the powder into a 20 mL glass vial and storing it in a glove box under an argon atmosphere.

The powders were consolidated into dense compacts using an induction hot-pressing technique (RIHP) described by Rangasamy *et al.* (Rangasamy *et al.* 2012) in a flowing argon atmosphere. The die assembly was subjected to a constant pressure of 23 MPa and heated to temperatures ranging from 900°C to 1100°C . For all hot-pressing runs, the max temperature was reached within 5 min ($180, 200, \text{ and } 220^\circ\text{C min}^{-1}$), and the samples were then held at that temperature ($900, 1000, \text{ and } 1100^\circ\text{C}$) for 1 h and cooled at 5°C min^{-1} . Each compact described in this paper was cut into slices using a diamond saw in oil (~ 1 mm thickness) and polished using 600, 1200, 1500 grit sand paper to $3 \mu\text{m}$, $0.3 \mu\text{m}$, and finally $0.05 \mu\text{m}$ finish using a lapper

(Southbay Technologies, Model 900). The polished slices, hereafter called hot-pressed pellets, were characterized to assess phase purity, morphology, and ionic conductivity.

2.2.2 Pellet Characterization

The pre-consolidated powder and hot-pressed pellets were analyzed using X-ray Diffraction (XRD) on a Bruker D8 DaVinci diffractometer equipped with Cu-K α X-ray radiation operating at 40 kV and 40 mA to investigate their crystal structure and phase purity. Rietveld refinement was used to analyze the XRD spectra and determine the volume percent of phases present. The relative density of each hot-pressed pellet was determined by measuring the mass and superficial geometric volume. The relative density values were determined by dividing the bulk density by the theoretical density (5.19 g cc⁻¹). The microstructural detail and morphology of all pellets were characterized using a Carl Zeiss EVO LS 25 scanning electron microscope (SEM) at 20 kV with an electron dispersive spectroscopy (EDS) attachment. The ionic transport was measured using an impedance analyzer (model SP-200 from Biologic Science Instruments) from 7 MHz to 1 Hz at room temperature. Platinum was sputtered on each face of the hot-pressed pellets as blocking-electrodes. The software program EC-Lab V10.30 was used for equivalent circuit modeling and each data set was normalized to the geometric dimensions of the pellet beforehand. Parameters were extracted from the equivalent circuit modeling, which were then used to generate simulated lines extrapolated to 7 GHz for both the 1000°C and 1100°C pellets. The modified equivalent circuit, based on work by Huggins(Huggins 2002), is shown in Figure 2.6. A constant phase element (CPE) was used to account for surface roughness and a mass transport element was used to account for the non-ideality of the blocking Pt electrodes. It is believed that a certain amount of dissolution of Li occurs within both electrodes. The 900°C pellet was modeled using the same equivalent circuit however the model didn't converge.

2.3 Results and Discussions

2.3.1 Effect of hot pressing temperature on phase purity and microstructure

Cubic $\text{Li}_6\text{La}_3\text{Zr}_2\text{Al}_{0.34}\text{O}_{12}$ (LLZO) powder + 10 wt% LLZO was hot pressed at 900, 1000, and 1100°C. In general, the X-Ray Diffraction (XRD) data indicated that cubic LLZO was the primary phase present; however, the hot pressing temperature did affect the fraction of secondary phases and the microstructure (Figure 2.1, and Table 2.1). Hot pressing at 900°C primarily resulted in cubic LLZO along with the formation of relatively small amounts of pyrochlore ($\text{La}_2\text{Zr}_2\text{O}_7$) and perovskite (LaAlO_3). Hot pressing at 1000°C resulted in cubic LLZO and a relative increase in pyrochlore ($\text{La}_2\text{Zr}_2\text{O}_7$) and perovskite (LaAlO_3) compared to the pellet pressed at 900°C. Hot pressing at 1100°C resulted in cubic LLZO with the highest phase purity among the samples investigated.

Previous reports (Rangasamy *et al.* 2012) indicated that when Li is lost during synthesis or sintering of LLZO, impurity phases form to maintain charge balance. As Li is lost, the impurity phase pyrochlore ($\text{La}_2\text{Zr}_2\text{O}_7$) and perovskite (LaAlO_3) typically form (Rangasamy *et al.* 2012, Huang *et al.* 2011). It has been observed that Li volatility increases with increasing sintering temperature, as observed by Huang *et al.* Although the trend that Huang *et al.* observed is consistent with the trend we observed from 900 to 1000°C, it is not consistent with the highest phase purity observed in the 1100°C pellet. We believe that the plateau hot pressing temperature does not affect the phase purity as much as it is the heating rate or the rate at which interconnected porosity collapsed to prevent Li loss. For example, the 900°C pellet was heated at 180°C min⁻¹, while the 1100°C pellet was heated at 220°C min⁻¹.

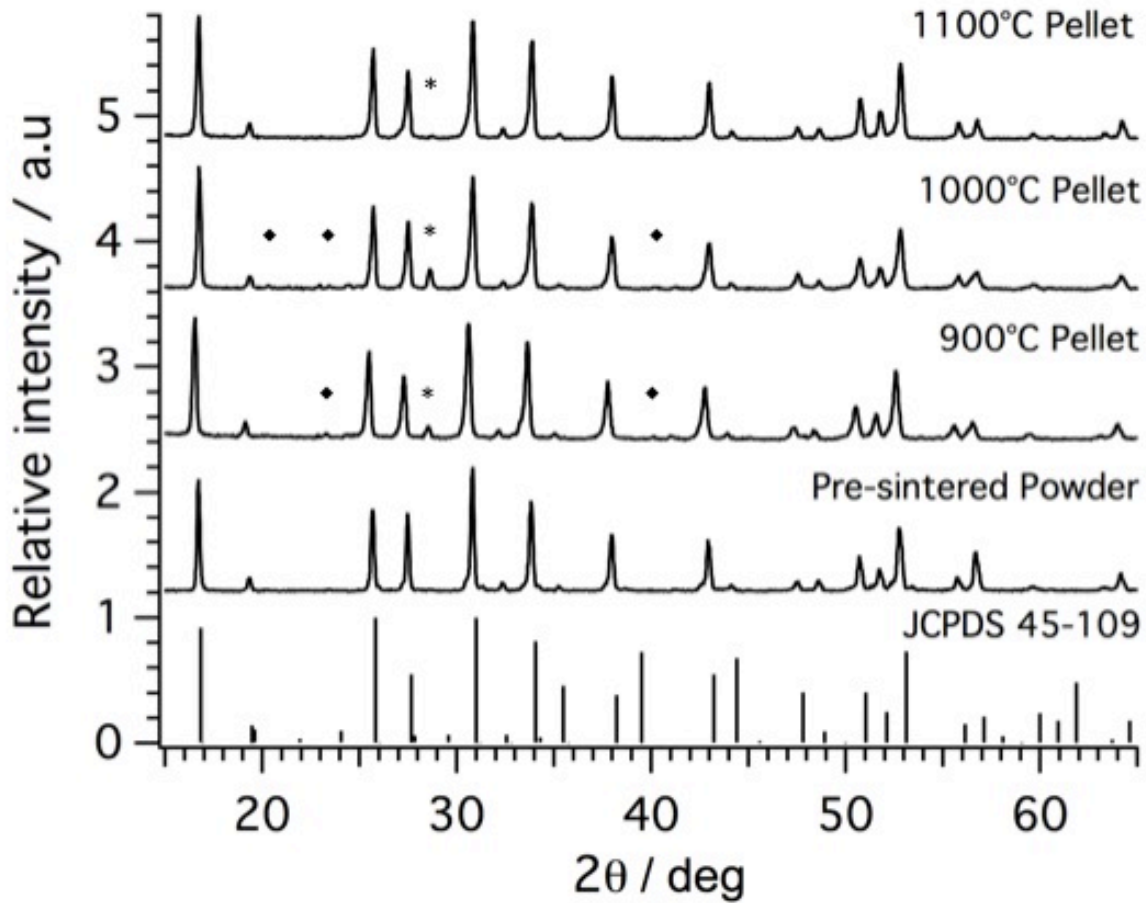


Figure 2.1 XRD patterns of the LLZO powder and hot-pressed pellets from 900°C to 1100°C, impurity phases are indicated by: * pyrochlore ($\text{La}_2\text{Zr}_2\text{O}_7$) and ♦ perovskite (LaAlO_3).

| Sample | Density (%) | Average grain size (μm) | Volume percent pyrochlore ($\text{La}_2\text{Zr}_2\text{O}_7$) | Volume percent perovskite (LaAlO_3) |
|---------|-------------|--------------------------------------|--|--|
| 900 °C | 86 | 1.9 | 2% | 3% |
| 1000 °C | 97 | 3.2 | 5% | 1% |
| 1100 °C | 99 | 4.6 | 1% | --- |

Table 2.1 Microstructural details of the hot-pressed LLZO pellets. The density was calculated after considering the contributions of impurity phases and porosity. The average grain sizes were calculated using the linear intercept method. The volume percent porosity was calculated using ImagePro software and the volume percent impurities were calculated using Rietveld refinement from the XRD spectra.

We hypothesize that because the 1100°C pellet was heated at the highest heating rate, pore collapse occurred the earliest in the heating cycle, thus reducing the amount of Li loss compared to the 900°C and 1000°C pellets. Furthermore, evidence of relatively more Li loss in the 1000°C pellet compared to the 900°C pellet could be explained by exposure to a relatively higher temperature, to accelerate Li loss, while taking longer for pore collapse to occur due to slower heating rates.

As expected, the hot pressing temperature increased the relative density (Table 2.1). The two pellets pressed at or above 1000°C had relative densities >95% (Table 2.1). The highest density (99%) was achieved in the 1100°C pellet, which is attributed to the highest hot pressing temperature. To our knowledge, this is the highest relative density ever reported for polycrystalline LLZO (Murugan *et al.* 2007; Huang *et al.* 2011; Buschmann *et al.* 2011; Rangasamy *et al.* 2012; Yutao Li *et al.* 2012). Our results indicate that hot pressing can achieve higher relative densities at relatively lower temperatures and in less time compared to conventional sintering.

The microstructural evolution of all three hot-pressed pellets, with respect to sintering temperature, is shown in Figures 2.2 and 2.3. The grain size, fraction of secondary phases and the reduction of porosity were characterized using scanning electron microscopy (SEM) on polished (Figure 2.2; backscattered electron micrographs) and fracture surfaces (Figure 3; secondary electron micrographs). From the SEM images, several observations can be made. First, the polished surface analysis (Figure 2.2)

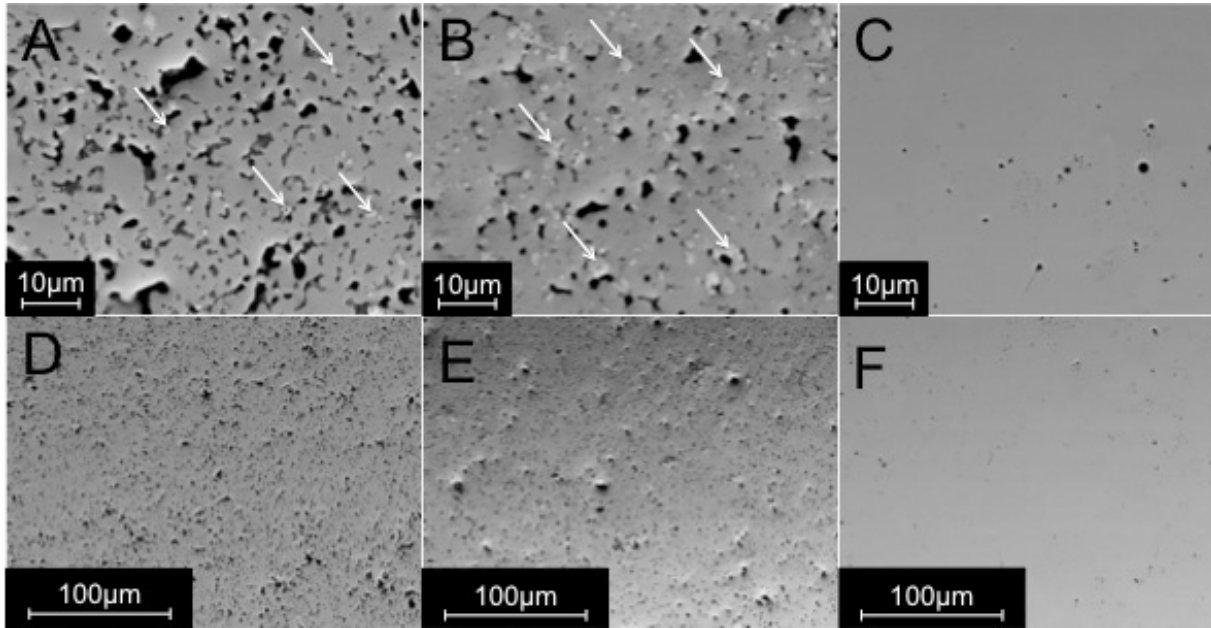


Figure 2.2 Backscattered electron SEM images of polished a,d) 900 °C b,e) 1000 °C and c,f) 1100 °C pellets, arrows point to the secondary phase pyrochlore ($\text{La}_2\text{Zr}_2\text{O}_7$). The polished surface images indicate as temperature increased, the pore shapes became spherical and the amount of porosity decreased.

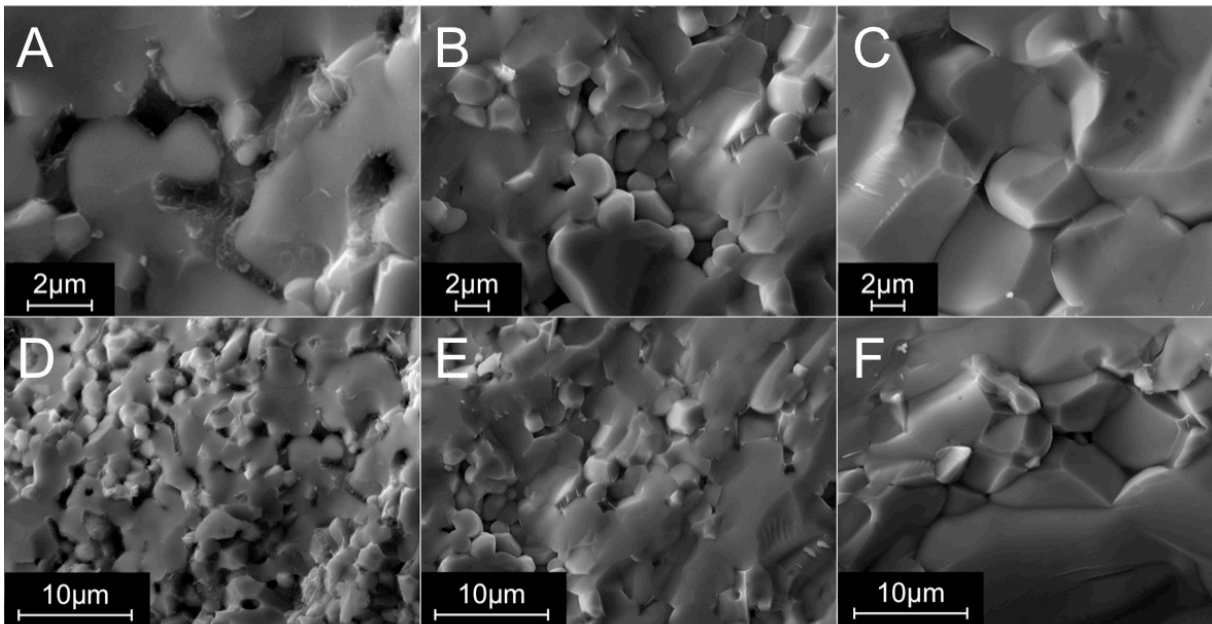


Figure 2.3 Secondary electron SEM images of fracture surfaces a,d) 900°C b,e) 1000°C and c,f) 1100°C pellets. The fracture surface images indicate as temperature increased, the amount of transgranular fracture and average grain size increased.

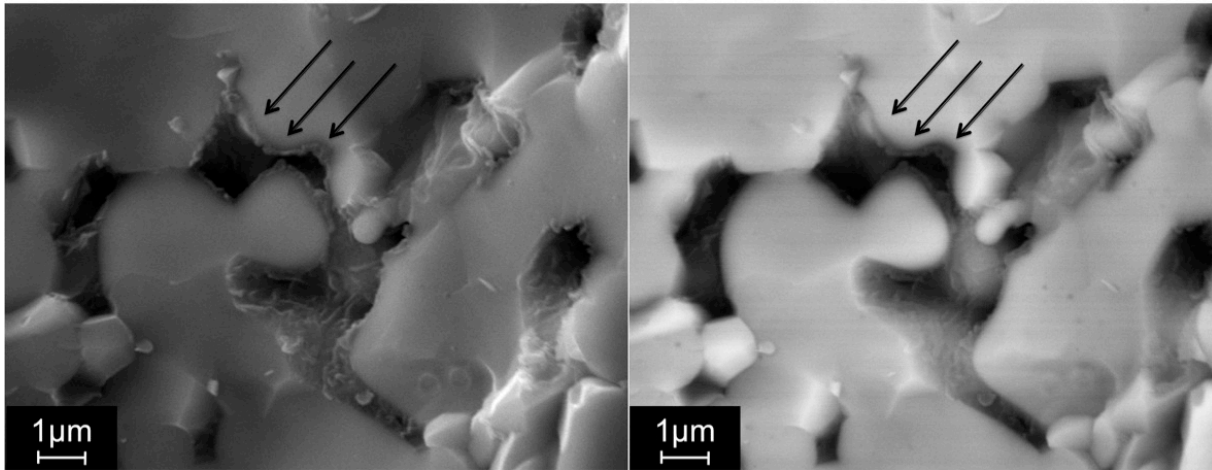


Figure 2.4 SEM analysis (24,000x) of the 900°C hot-pressed pellet with a) secondary electrons and b) backscattered electrons, arrows point to the film visible on all the internal pores surfaces.

indicated that increasing the hot pressing temperature increased the relative density (Figure 2.2a to 2.2c). For the pellets hot pressed at 900°C and 1000°C, the pore morphology is consistent with intermediate phase sintering where pore coalescence is not complete. (Barsoum 2002) In comparison, the pellet hot pressed at 1100°C consisted of a more homogenous microstructure with a relatively low volume fraction of pores more consistent with the final stage of sintering where the pores are relatively small and isolated (Figure 2.2c,e). (Barsoum 2002) Second, the phase purity increased with increasing hot pressing temperature. The lighter features, indicated by the arrows in Figure 2.2(a,b), are evidence of a secondary phase with a higher average Z number. We assume that the secondary phase is primarily pyrochlore ($\text{La}_2\text{Zr}_2\text{O}_7$), because the average Z number is higher than LLZO and perovskite (LaAlO_3). Additionally, when energy dispersive spectroscopy (EDS) was conducted on these lighter phases at low magnifications of 1000x – 2000x, an estimated 1:1 ratio of La to Zr indicated the presence of pyrochlore, which has a 2:2:7 La:Zr:O ratio. Although the resolution of EDS was not sufficient to confirm the secondary phase precise stoichiometry, a quantitative comparison indicates the secondary phase

fraction is highest in the pellet hot pressed at 1000°C, slightly lower in the pellet hot pressed at 900°C and not detectable in the pellet hot pressed at 1100°C. This qualitative analysis is consistent with the quantitative Rietveld refinement data (Table 2.1), confirming the same trend between the hot pressing temperature and fraction of secondary phase(s). Third, the grain size increased and fracture mode transitioned from inter to intragranular fracture with increasing hot pressing temperature (Figure 2.3 and Table 2.1). The average grain size increased from 1.9 μm to 4.6 μm when hot pressing at 900 and 1100°C, respectively.

2.3.1.1 Anomalous behavior in the 900°C pellet

The pellet hot pressed at 900°C had unique microstructural features. First, the surface of grains that terminated in pores were coated with a relatively thin (~few hundred nm) film (Figure 2.4a and b). Figure 2.4a is a secondary electron topographical image clearly showing the shape and distribution of the coating on all internal surfaces. Figure 4b is a backscattered electron image distinguishing the two dissimilar phases into the lighter grey LLZO with a higher average Z number and darker grey film on all internal surfaces. The film has been characterized using EDS and is consistent with a relatively low average Z compound that we speculate could be Li₂CO₃, though this technique has limitations in that Li cannot be detected. The presence of Li₂CO₃ could be related to what is hypothesized above regarding Li loss. Because the pellet pressed at 900°C took the longest (compared to the pellets hot pressed at 1000 and 1100°C) to reach a temperature to collapse pores, Li in the LLZO could have reacted with CO or CO₂, evolved from the graphite dies, to form Li₂CO₃ on exposed particle surfaces. Additionally, the XRD spectra for the pellet hot pressed at 900°C (Figure 2.1) did not indicate the presence of

Li_2CO_3 peaks. However, because the Li_2CO_3 was relatively thin, or the volume fraction was low, it may not have been detected using XRD.

2.3.2 Electrochemical Impedance Spectroscopy (EIS)

Room temperature EIS was conducted on the all three hot pressed pellets (Figures 5 and 6). In Figure 5, the markers and black lines indicate the experimental results and equivalent circuit modeling, respectively. The equivalent circuit modeling results were used to simulate the impedance spectra to higher frequencies so that the characteristic frequencies for the 1000°C and 1100°C samples (Figure 2.6) could be determined. Interpretation of the transport phenomena in the 900°C pellet was complex due to the multiple phases present at the grain boundaries (Figure 2.4a,b). This complexity made it difficult to analyze the phenomenon associated with each element of the equivalent circuit. As observed by Hsieh *et al.* (Hsieh & DeJonghe 1978) and De Jonghe *et al.* (De Jonghe 1979), modeling complex grain boundaries with non-uniform thickness is challenging and beyond the scope of this work.

The impedance analysis in this study is focused on the pellets hot-pressed at 1000°C and 1100°C . The Nyquist plots (Figure 2.5 and 2.6) can be separated into two distinct regions: 1) the bulk and grain boundary processes at the high-frequency portion of the spectrum 2) the lower frequency processes or vertical tails related to the Li-ion blocking electrode behavior. The results of the impedance data fitting include Q-values, alpha values, percent grain boundary contribution, and the bulk and total conductivities (Table 2.2). The grain boundary contribution is lower as the sintering temperature was increased as observed in Table 2.2. The reported total conductivity is a sum of the bulk and grain boundary contributions.

As seen in the SEM micrographs, the higher density and relatively larger grains in the both 1000°C and 1100°C compared to the 900°C pellet manifested as low grain boundary resistances for both pellets (Figure 2.6). The significantly lower grain boundary resistances in the 1000 and 1100°C pellets enabled measurement of their bulk ionic conductivities (Table 2.2). The Q-values for the grain boundary and bulk transport for both the 1000 and 1100°C pellets are similar and are relatively consistent with the values expected for a bulk process. (Huggins 2002; Irvine *et al.* 1990) The alpha value for the grain boundary transport in the 1000°C pellet refine to 0.75 which is somewhat consistent with what is predicted by the equivalent circuit model. For the 1100°C the grain boundary alpha refines to exactly 1.0 which indicates the grain boundary transport is in excellent agreement with the constant phase element used to model idealized grain boundary transport. But for the 1000°C the grain boundary is behaving less ideally which could be corroborating the fracture mode analysis where the grains are not as well connected compared to the 1100°C pellet.

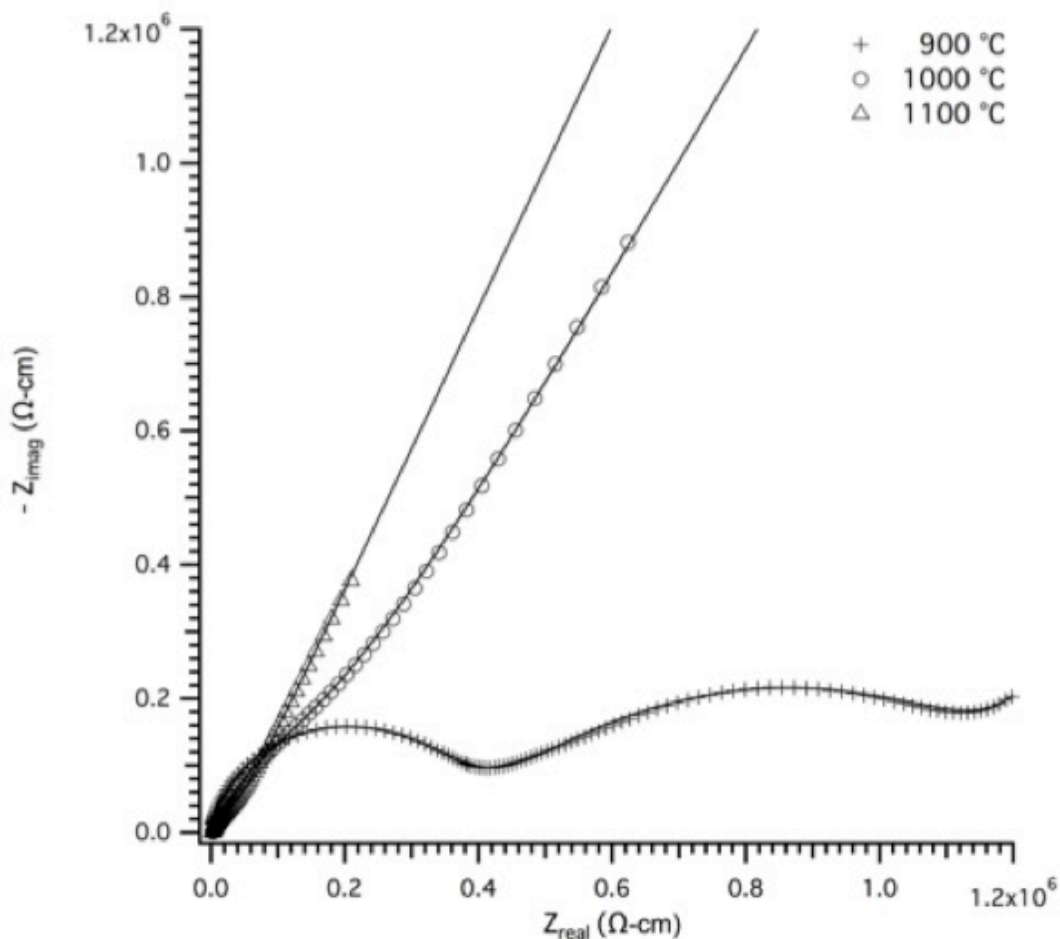


Figure 2.5 Impedance plot (7 MHz – 1 Hz) of hot-pressed LLZO pellets at various sintering temperatures. Markers indicate experimental data and the solid lines, for the 1000°C and 1100°C pellets, are simulated lines extrapolated from the best-fit line.

| Sample | Q_{bulk} | α_{bulk} | σ_{bulk} [mS cm ⁻¹] | Q_{gb} | α_{gb} | $\frac{R_{\text{gb}}}{R_{\text{gb}} + R_{\text{bulk}}}$ | σ_{total} [mS cm ⁻¹] |
|--------|-----------------------|------------------------|--|----------------------|----------------------|---|---|
| 1000°C | 2.8×10^{-11} | 0.915 | 0.36 | 5.8×10^{-8} | 0.752 | 26% | 0.27 |
| 1100°C | 1.8×10^{-11} | 0.923 | 0.41 | 1.9×10^{-8} | 1.00 | 8% | 0.37 |

Table 2.2 Electrochemical properties of hot-pressed 1000°C and 1100°C LLZO pellets. The Q_{gb} , Q_{bulk} , α_{gb} , and α_{bulk} represent the Q-values and α 's for both the grain boundary and bulk. The % grain boundary contribution to the total conductivity is seen here in column 6. The bulk and total conductivities are reported based on values from the best-fit data. The total conductivity reported is the sum of the bulk and gb resistivities, normalized by geometric dimensions during equivalent circuit modeling.

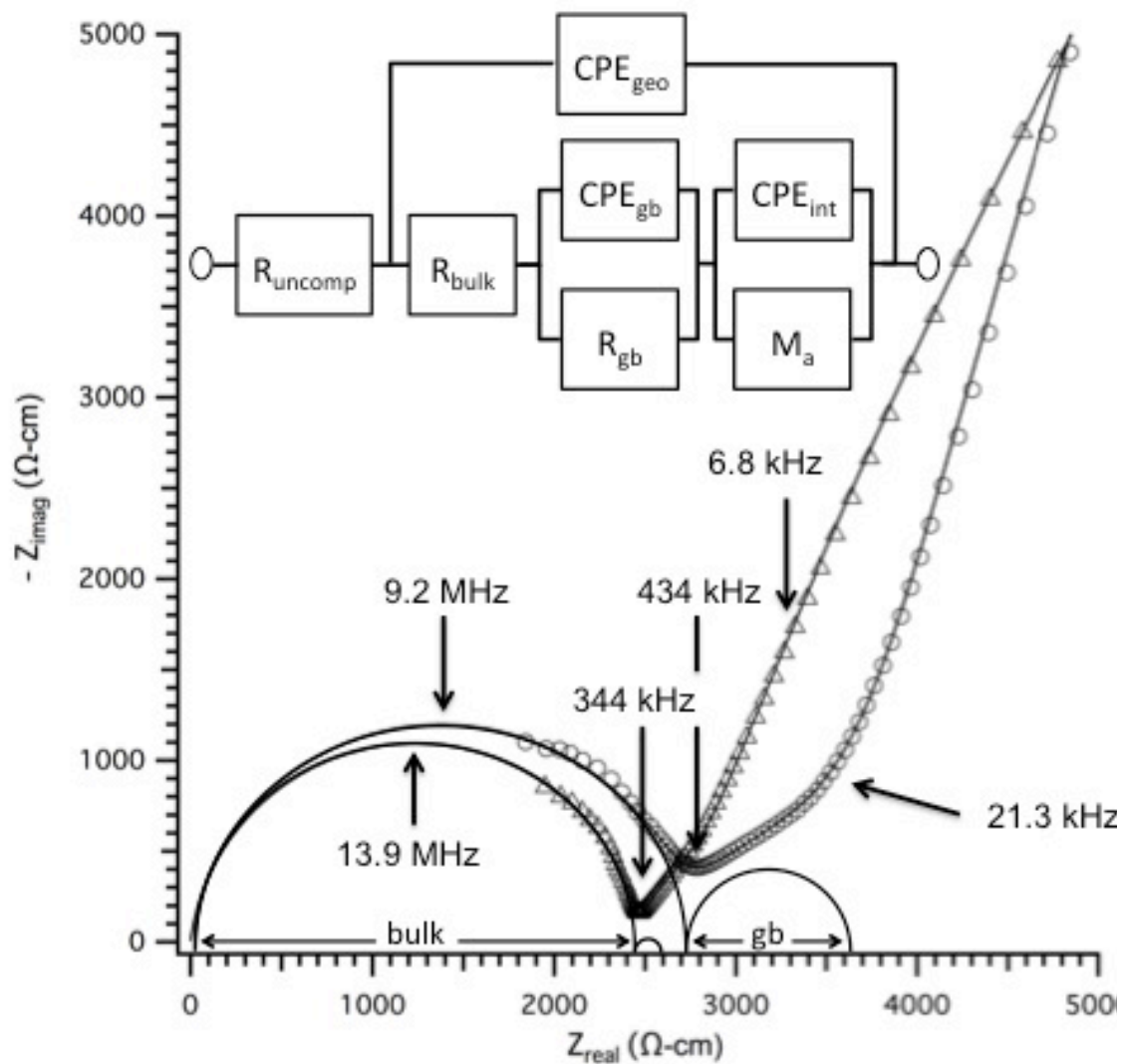


Figure 2.6 Impedance plot of 1000°C (circles) and 1100°C (triangles) hot-pressed LLZO pellets at high frequency. Markers indicate experimental data and the solid lines are simulated lines extrapolated from the equivalent circuit modeling using the equivalent circuit shown here. R and CPE refer to the resistance and constant phase element and the subscripts uncomp, geo, gb, int represent uncompensated, geometric dimensions, grain boundary, and interfaces. The frequencies presented, from left to right, indicate the characteristic frequency, bulk, and electrode processes. The semi-circles (left to right) represent the bulk and gb resistivities for the 1000°C and 1100°C pellets respectively.

Improving the ionic conductivity of LLZO has been previously investigated through pressure-less sintering (Ban & Choi 2001; Awaka *et al.* 2009; Huang *et al.* 2011) and hot-pressing techniques (Wolfenstine *et al.* 2012; Rangasamy *et al.* 2012) achieving total ionic conductivities ranging from $1.4 - 4.0 \times 10^{-4} \text{ S cm}^{-1}$ (Murugan *et al.* 2007; Buschmann *et al.* 2011; Kumazaki *et al.* 2011; Yutao Li *et al.* 2012; Rangasamy *et al.* 2012). Reducing grain boundary resistance has been observed here by applying pressure during sintering. Hot-pressing cubic Al doped LLZO at different sintering temperatures has increased particle-to-particle contact, leading to lower grain boundary resistance, and higher total conductivity without the addition of other dopants. Kumazaki *et al.* (Kumazaki *et al.* 2011) and Rangasamy *et al.* (Rangasamy *et al.* 2012) have suggested that the lack of a clear second semi-circle, associated with grain boundary conduction, in the pellet with the highest conductivity results from nearly removing all grain boundary resistance in this pellet. Based on the EIS data it is apparent the 1100°C pellet exhibits one of the lowest grain boundary resistances ever reported for LLZO (8 % of the total resistance) demonstrating the need to increase grain size and decrease porosity to maximize the total ionic conductivity. Future work will entail characterizing the mechanical properties as a function of porosity and grain size to enable the fabrication of thin, high conductivity LLZO membranes.

2.4 Conclusion

The effect of hot pressing temperature on the microstructure and Li-ion transport of $\text{Li}_6\text{La}_3\text{Zr}_2\text{Al}_{0.34}\text{O}_{12}$ (LLZO) was investigated. It was determined that hot pressing at 900°C resulted in the lowest relative density (86 %), ~ 5% impurity phases, and anomalously low total ionic conductivity. Compared to the pellet hot pressed at 900°C, the pellets pressed at 1000 and

1100°C resulted in significantly higher relative densities and total ionic conductivities. The 1000 and 1100°C pellets had 97, and 99 % relative densities and 0.27 and 0.37 mS cm⁻¹ total ionic conductivities at room temperature, respectively. Because the difference in relative density was small when comparing the pellets hot pressed at 1000 and 1100°C (97 % vs 99%), we attribute the 27% increase in total conductivity to the increase in grain size (3.2 and 4.6 mm, respectively) and higher phase purity (6% vs. 1 % phase impurities, respectively).

2.5 Acknowledgements

ID, TT, and JS would like to acknowledge the support from the Tank and Automotive Research and Development Engineering Center in Warren, MI and the U.S. Army Research Office, grant W911NF-13-1-0475. JW would like to acknowledge support of the U. S. Army Research Laboratory (ARL).

3. Liquid phase sintering of $\text{Li}_{6.22}\text{La}_3\text{Zr}_2\text{Al}_{0.26}\text{O}_{12}$ with the sintering aid Tri-isopropyl borate

3.1 Introduction

Superionic conducting oxide (SCO) electrolytes are a promising alternative to liquid electrolytes for lithium ion batteries because they may reduce safety hazards and costs. Solid electrolytes must have relatively high density to improve ionic conduction and mechanical properties such as fracture toughness and strength. It has been shown in several systems that grain boundary resistances can reduce the total ionic conductivity by two orders of magnitude (10^{-3} to 10^{-5} S cm⁻¹). One approach to improve the density is by reducing the initial particle size of the powder to enhance densification. (Mariappan *et al.* 2011) Mariappan *et al* suggest that

the grain size itself is not responsible for grain boundary effects, but instead that the grain boundary thickness is the more important factor. These results imply that it is necessary to introduce a processing technique such as liquid phase sintering via the addition of a conductive sintering aid to reduce the grain boundary resistance, which has the added benefit of possibly reducing the sintering temperature as well. Upon cooling, this second phase will either crystallize or form a glassy phase that surrounds all the small grains and bonds them together. This will reduce the porosity and secondary phase formation that has been shown to aggregate at the triple points.

LLZO is a promising SCO electrolyte for Lithium ion batteries because it exhibits the unique combination of conductivity, shear modulus, stability and has been shown to achieve up to 99% relative density when sintered at 1100°C. In spite of this success, the need for reaching such high temperature makes this specific approach impractical for long-term solid electrolyte manufacturing practices. Commercial applications such as electric vehicles and other energy storage technologies have outlined some guidelines for research, in that it is necessary to reduce the sintering temperature in order to minimize energy consumption during processing. To attain high densities at lower sintering temperatures, it has been proposed that sintering aids with low melting temperatures may initiate liquid phase sintering and enhance sintering kinetics.(Aono *et al.* 1990; Ohta *et al.* 2013; Yiqiu Li *et al.* 2013; Tadanaga *et al.* 2013) Preliminary investigations of pressureless sintering of ceramic electrolytes indicate that relative densities greater than 95% can be achieved at a sintering temperature of 900°C with various sintering aids such as LiPO₃(Hu *et al.* 1976; Aono *et al.* 1990), LiO₂(Aono *et al.* 1990; Aono *et al.* 1991; Yiqiu Li *et al.* 2013), and Li₃BO₃(Aono *et al.* 1990; Ohta *et al.* 2013; Tadanaga *et al.* 2013; Takano *et al.*

2014). For example, Hu *et al.* reported in 1976 that the ionic conductivity can be increased in hot pressed Li_4SiO_4 from $1.3 \times 10^{-9} \text{ S cm}^{-1}$ to $1.0 \times 10^{-4} \text{ S cm}^{-1}$ with the addition of 40mol% Li_3PO_4 .(Hu *et al.* 1976) In another solid electrolyte system, Aono *et al* sintered NASICON-type electrolytes with several lithium salt sintering aids. Their study indicated that the lowest porosity pellets were achieved with $\text{LiTi}_2(\text{PO}_4)_3 - X\text{Li}_3\text{BO}_3$ ($0.3 < X < 0.75$). According to their results, the high density in the $\text{LiTi}_2(\text{PO}_4)_3 - 0.2\text{Li}_3\text{BO}_3$ system is the main reason for the ionic conductivity enhancement. This work expands on these results by examining the effects of adding tri-isopropoxy borate (TIB) into a $\text{Li}_{6.22}\text{La}_3\text{Zr}_2\text{Al}_{0.26}\text{O}_{12}$ (LLZO) + 32 wt% ex Li_2CO_3 ceramic system during conventional solid-state synthesis. Various weight percentages of the additive were mixed in and hot pressed to study whether this addition may allow for an increase in the density of LLZO at a lower sintering temperature. The effects of hot pressing on the LLZO phase, microstructure, and ionic conductivity were examined to test this concept.

3.2 Experimental Methods

3.2.1 Powder Preparation and Hot-Pressing Technique

Samples of $\text{Li}_{6.22}\text{La}_3\text{Zr}_2\text{Al}_{0.26}\text{O}_{12}$ (LLZO) + 32 wt% ex Li_2CO_3 were prepared by solid-state reaction similar to that described by refs (Rangasamy *et al.* 2012; Murugan *et al.* 2007; Huang *et al.* 2011). The raw materials of Li_2CO_3 (Alpha Aesar, Ward Hill, MA), $\text{La}(\text{OH})_3$ (Alpha Aesar), Al_2O_3 (Mager Scientific Inc, Dexter, MI), and Zr_2O_3 (Inframat® Advanced Materials, Manchester, CT) were weighed and combined in an agate vial according to the desired stoichiometric ratio. This powder mixture was dry-milled in a planetary mill for 4 h at 350 rpm, then uniaxially pressed (100 MPa) into pellets in a 1” stainless steel die and calcined three times

at 1000°C for 4 h at a heating rate of 100°C hr⁻¹. The calcined pellets were then ground by hand with a mortar and pestle to form a loose powder.

Experiments were performed on four samples. The samples were stored in 20 mL vials in a low-humidity room (a dry room with a -72 F dewpoint), with each vial containing 2.7 g of calcined LLZO powders. Varying amounts of a 10:1 anhydrous isopropanol (Alpha Aesar): triisopropoxy borate (Alpha Aesar) stock solution (TIB) were added to each vial, at weight percent ratios of X = 0, 1, 2, and 5. Each vial was mixed in a 125 mL agate mixing-vial for 20 min at 400 rpm. After mixing, each LLZO powder + X wt% TIB slurry was poured into a glass petri dish and left to dry for 2 h under ambient conditions. Each sample was then pelletized into a ½” diameter stainless steel die and calcined at 450°C for 4 h at a heating rate of 100°C hr⁻¹. The resulting calcined compacts were then individually ground with a mortar and pestle, and the powders of each sample were collected into separate 20 mL glass vials and stored in a glove box under an argon atmosphere.

The powders were consolidated into dense compacts using an induction hot-pressing technique (RIHP) described by Rangasamy *et al.* (Rangasamy *et al.* 2012) in a flowing argon atmosphere. The die assembly was subjected to a constant pressure of 23 MPa and heated to 900°C at a heating rate of 200°C min⁻¹ and held for 1 h at temperature. The samples were then cooled at 5°C min⁻¹. Each compact described in this paper was cut into slices using a diamond saw in oil (~1 mm thickness) and polished using 600, 1200, 1500 grit sand paper to 3 μm, 0.3 μm, and finally 0.05 μm finish using a lapper (Southbay Technologies, Model 900). The polished slices, hereafter called hot-pressed pellets, were characterized to assess phase purity,

morphology, and ionic conductivity. A schematic of the experimental methods has been provided (Figure 3.1).

3.2.2 Pellet Characterization

The decomposition behavior of mixed and dried LLZO + 5 wt% TIB powder was analyzed using thermogravimetric analysis (TGA) to determine the first heat treatment temperature. TGA and DSC measurements were performed on a Netzsch STA 449 F3 Jupiter at a heating rate of $5^{\circ}\text{C min}^{-1}$ in a N_2 atmosphere. The pre-sintered powder and hot-pressed pellets were analyzed using X-ray Diffraction (XRD) on a Bruker D8 DaVinci diffractometer equipped with $\text{Cu-K}\alpha$ X-ray radiation operating at 40 kV and 40 mA to investigate their crystal structure and phase purity.

The density of each hot-pressed pellet was determined by measuring the mass and volume. The relative density values were determined by dividing the bulk density by the theoretical density. The microstructural detail and morphology of all pellets were characterized using a Carl Zeiss EVO LS 25 scanning electron microscope (SEM) at 20 kV for polished surface micrographs and a dual column focused ion beam (FIB)-SEM (Carl Zeiss Auriga CrossBeam) for fracture surface imaging. The ionic transport was measured using an impedance analyzer (model SP-200 from Biologic Science Instruments) from 7 MHz to 1 Hz at room temperature. Platinum was sputtered on each surface of the hot-pressed pellets as blocking-electrodes. The software program EC-Lab V10.30 was used for data fitting (in the range 7 MHz to 1 Hz) and each data set was normalized to the geometric dimensions of the pellet beforehand.

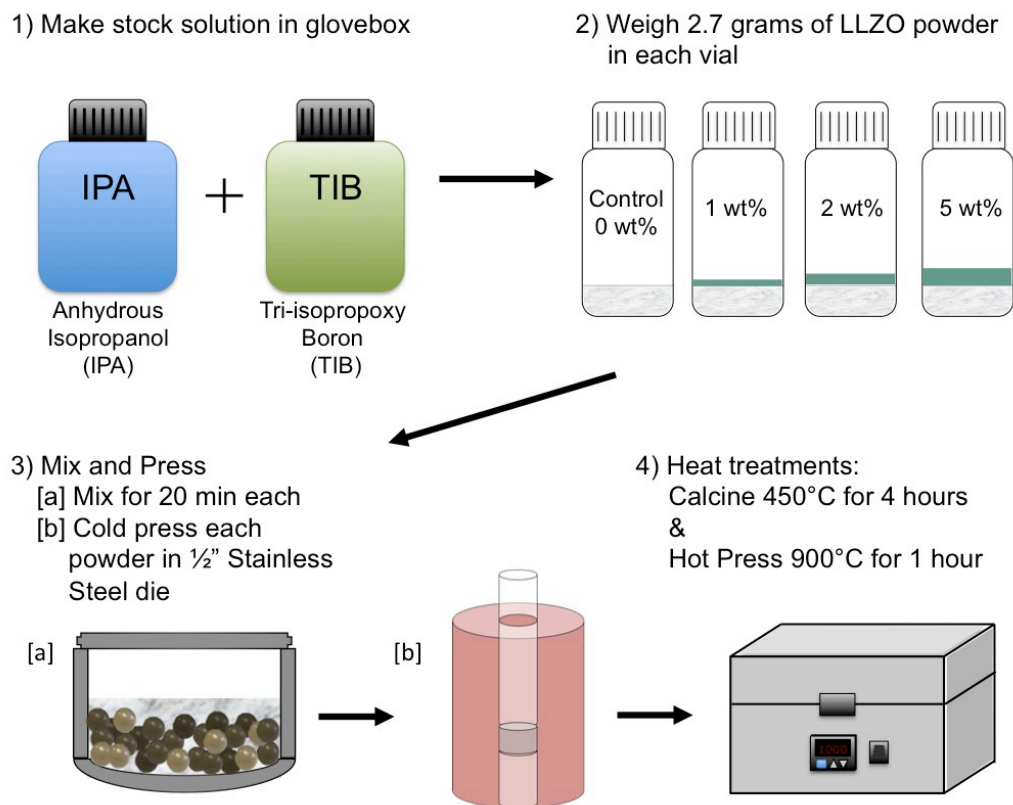


Figure 3.1 Schematic of LLZO + TIB powder synthesis/processing

Parameters were extracted from the equivalent circuit modeling. The modified equivalent circuit, based on work by Huggins(Huggins 2002) is shown in Figure 3.9. A constant phase element (CPE) was used to account for surface roughness and a mass transport element was used to account for the non-ideality of the blocking Pt electrodes. It is believed that a certain amount of dissolution of Li occurs within both electrodes.

3.3 Results and Discussion

3.3.1 Thermogravimetric analysis (TGA), Differential scanning calorimetry (DSC), and X-Ray Diffraction (XRD)

TGA/DSC was conducted on as-milled and dried LLZO + 5 wt% TIB powder in the temperature range from room temperature to 1200°C (Figure 3.2) in a nitrogen atmosphere. The

TGA curves exhibit two weight loss steps up to 1200°C. The first mass loss is most likely due to evaporation of moisture or moieties from the precursor powder after mixing and subsequent drying of TIB in the LLZO matrix. This happens near ~ 420°C and is associated with the melting and vaporization of B₂O₃, which has a melting temperature of 450°C.(Tamura *et al.* 1999) The second distinct mass loss corresponds to the DSC peak around 675°C. This peak in the DSC coincides with a lithium borate eutectic formation range in the Li₂O-B₂O₃ phase diagram (Figure 3.3).

According to Matthews *et al*, high-temperature lithium borate phases are sensitive to heat treatments above 675°C.(Mathews *et al.* 1998) According to the phase diagram (Figure 3.3), the hot pressing temperature of 900°C is consistent with Li₂B₄O₇ which is a stable phase that melts and cools as a congruent glassy phase.(Sastry & Hummel 1959; Mathews *et al.* 1998) In this study, it is possible that small amounts of lithium borate formed at the grain boundaries but it is unclear what composition precipitated. As will be discussed in the next section, it is difficult to detect lithium or boron. Several groups have used X-ray Diffraction or Neutron diffraction to identify lithium borate compositions, however, the low atomic mass of both lithium and boron as well as the absorbance of neutrons by boron limit applicability of these techniques.(Rousse *et al.* 2014) The next section will focus on identifying the structural change of LLZO using X-ray diffraction.

XRD was performed for each stage of LLZO/TIB synthesis and processing: 1) As-synthesized LLZO powder after 3 calcination heat treatments of 1000°C for 1 h (100°C h⁻¹ heating rate) (Figure 3.4a); 2) after each 2.7 g sample went through a precalcination step of

450°C for 4 h (Figure 3.4 b – e); and 3) on each hot pressed pellet after polishing the surface down to a 0.05 µm finish (Figure 3.5 c – f). XRD was conducted on all stages of synthesis and processing to investigate the phases present before the addition of TIB and after both the furnace heat treatment of 450°C and hot pressing at 900°C. For the as-synthesized powder, the diffraction pattern is consistent with the expected tetragonal phase (Rangasamy *et al.* 2012; Jin & McGinn 2011; Awaka *et al.* 2009). After the first heat treatment at 450°C, peak distortions around 17, 27.5, and 43 (2θ) suggest that a small degree of structural change occurred within the samples with additions of TIB. Unlike the LLZO + 1, 2, and 5 wt% TIB samples, the peaks in the XRD spectra of the LLZO + 0wt% sample remained consistent with the as-synthesized tetragonal LLZO powder.

The second heat treatment at 900°C significantly affected the structure of all hot pressed samples (Figure 3.5). The peaks observed in the XRD spectra after hot pressing are more consistent with the cubic garnet structure in Figure 3.5a. The structural change after the second heat treatment was most apparent in the LLZO + 1, 2, and 5wt% TIB samples. Along with the structural change from tetragonal to cubic LLZO, small amounts of pyrochlore (La₂Zr₂O₇) and perovskite (LaAlO₃) precipitated during the second heat treatment. These impurity phases are consistent with other reports of Li-loss during high temperature heat treatments of LLZO above 900°C.(Tadanaga *et al.* 2013; Takano *et al.* 2014; Rangasamy *et al.* 2012)

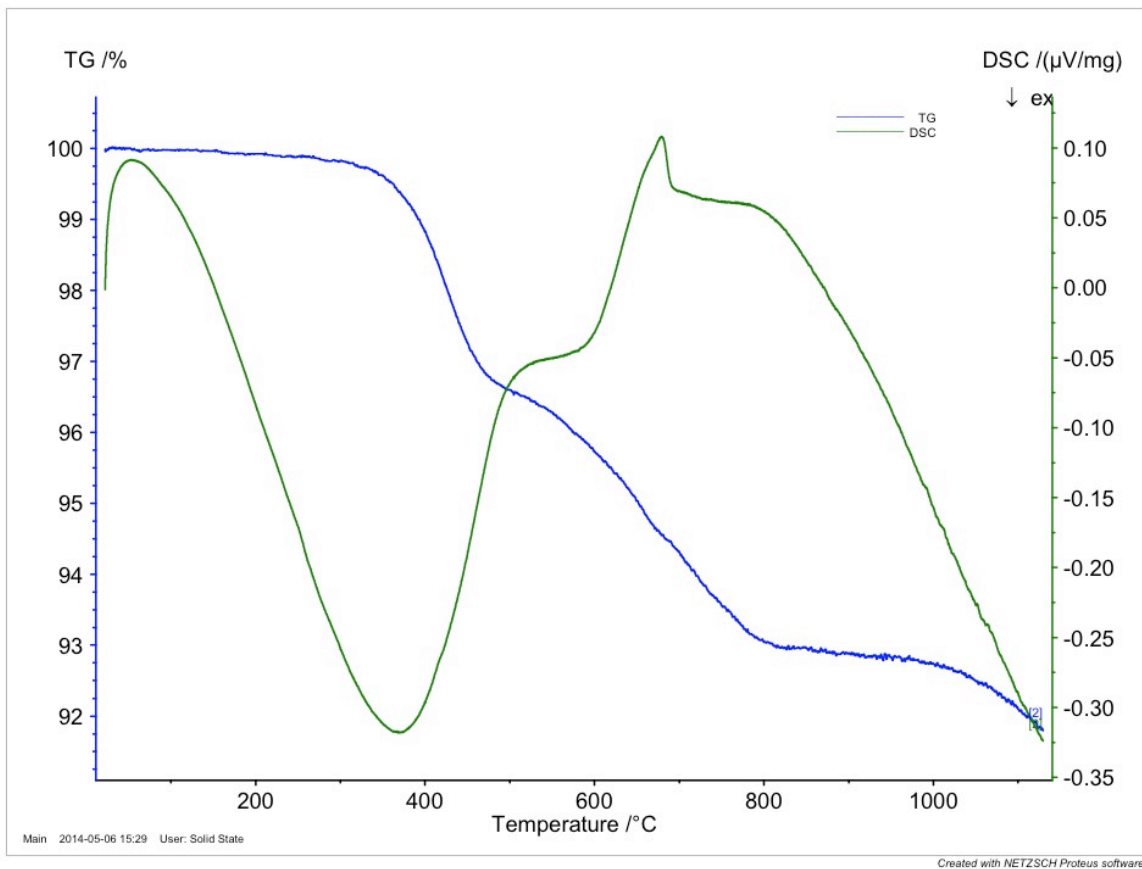
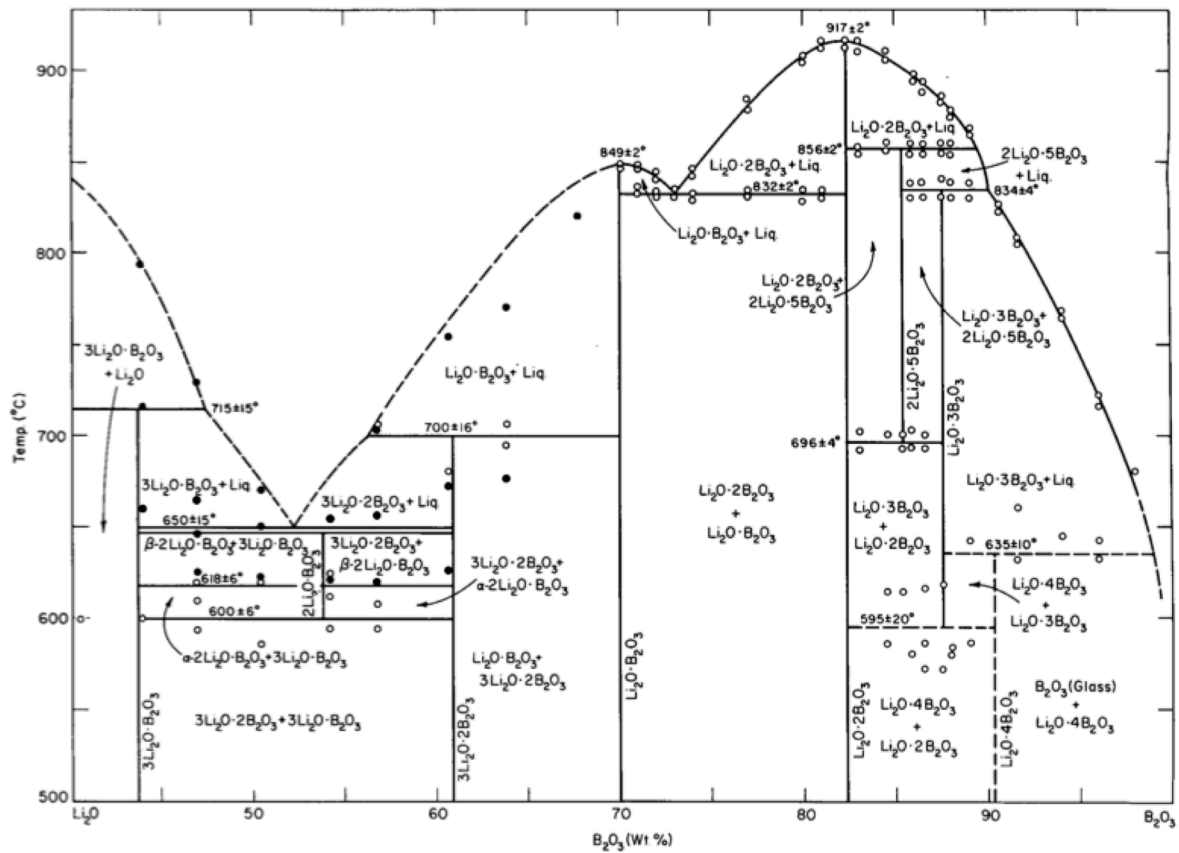


Figure 3.2 Thermogravimetric analysis (green) and Differential scanning calorimetry (blue) on LLZO + 5 wt% TIB in the temperature range 25°C to 1200°C in a nitrogen atmosphere at 5°C min⁻¹

Fig. 1. The system $\text{Li}_2\text{O}-\text{B}_2\text{O}_3$.Figure 3.3 Phase diagram for Li_2O and B_2O_3 from Sastry *et al.* (Sastry & Hummel 1959)

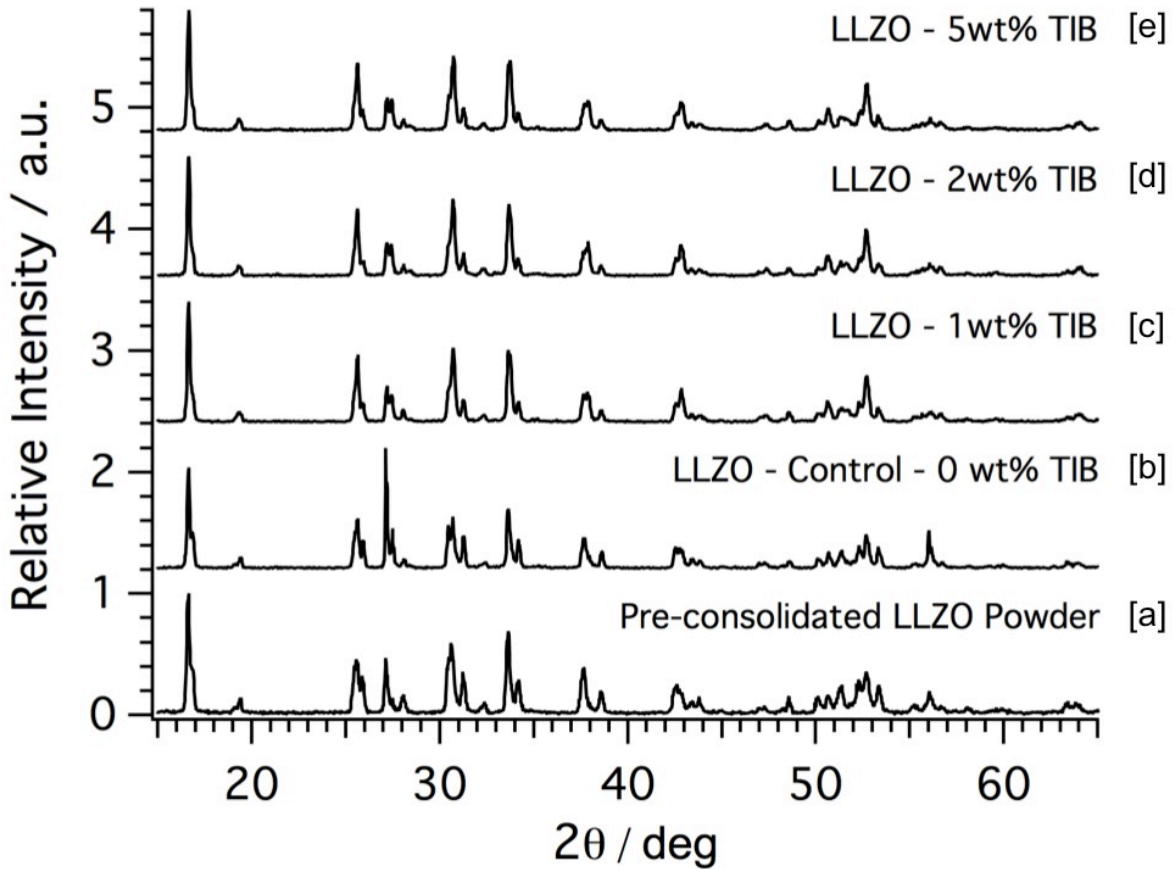


Figure 3.4 X-ray diffraction of the as-synthesized powder (a) and the four samples after the first heat treatment at 450°C. b) Control sample c) 1wt% TIB d) 2wt% TIB e) 5wt% TIB. The XRD spectra of the pre-consolidated LLZO powder are consistent with tetragonal garnet phase (Rangasamy *et al* 2012). After the 450°C heat treatment, peak distortions around 17, 27.5, and 43 (2θ) suggest that a small degree of structural change occurred within the samples with additions of TIB.

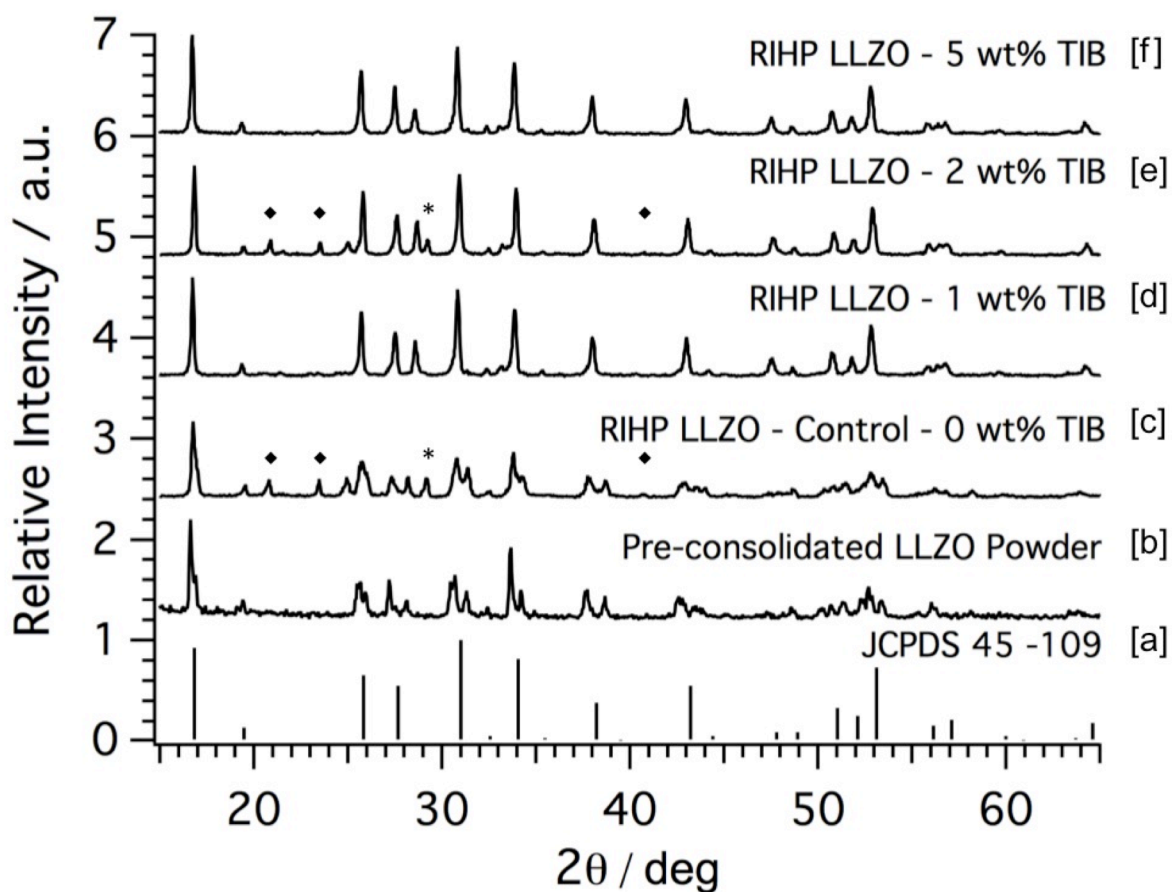


Figure 3.5 XRD of the LLZO + TIB samples after hot pressing at 900°C. a) JCPDS 08-457 b) Pre-consolidated LLZO powder c) Control sample d) 1wt% TIB e) 2wt% TIB and f) 5wt% TIB. Impurity phases are indicated by: * pyrochlore ($\text{La}_2\text{Zr}_2\text{O}_7$) and ♦ perovskite (LaAlO_3). The pre-sintered LLZO powder (b) is consistent with tetragonal garnet (Rangasamy *et al* 2012) while the XRD peaks in (c – f) are consistent with the JCPDS 45-109 cubic garnet phase.

3.3.2 Density and Microstructural analysis

Scanning electron microscopy (SEM) was conducted on the fracture surface and polished surface of each hot pressed sample. A change in relative density can be observed in both the polished and fracture surface SEM images (Figures 3.6, 3.7 and 3.8) where the amount of porosity decreases with the increase of TIB addition. For the LLZO + 0wt% TIB sample, both the fracture surface and polished surface SEM images depict the initial stage of solid state sintering without an additive. Moreover, in the fracture surface images (Figure 3.7a and 3.8a) the particle-to-particle contact is relatively poor compared to the samples with TIB. For the samples with TIB additions, a secondary phase surrounded the grains of LLZO in the fracture surface images (Figure 3.7). Also with increasing TIB addition, a visibly thicker coating of this secondary phase surrounds each particle as well as separates the particles from each other. The secondary phase can be clearly distinguished from the LLZO particles in the 1 wt% TIB sample (Figure 3.8 b, c, and d). The particle-to-particle contact in both the 1 and 2 wt% TIB samples appear to be much better than the control sample as seen from the slight distortion of the surface of each particle (Figure 3.8c). For the LLZO + 1, 2, and 5 wt% TIB samples, fracture surface SEM images (Figure 3.8 a-d) at high magnification indicate microstructures that have grains with faceted surfaces. However, in the 5 wt% TIB sample, the coating has nearly separated all particles from each other so a flat fracture surface limits the visibility of the individual particles.

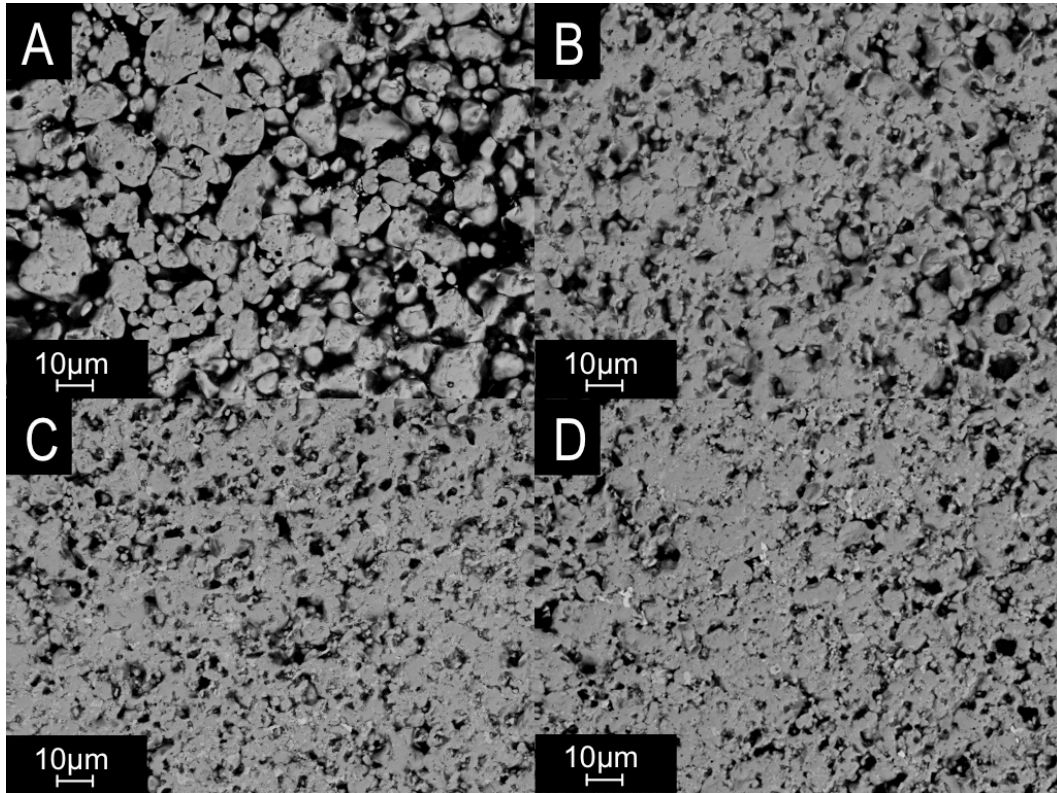


Figure 3.6 SEM polished surface images (backscattered electrons) at 2000x of a) 0 wt% TIB b) 1 wt% TIB c) 2 wt% TIB and d) 5 wt% TIB

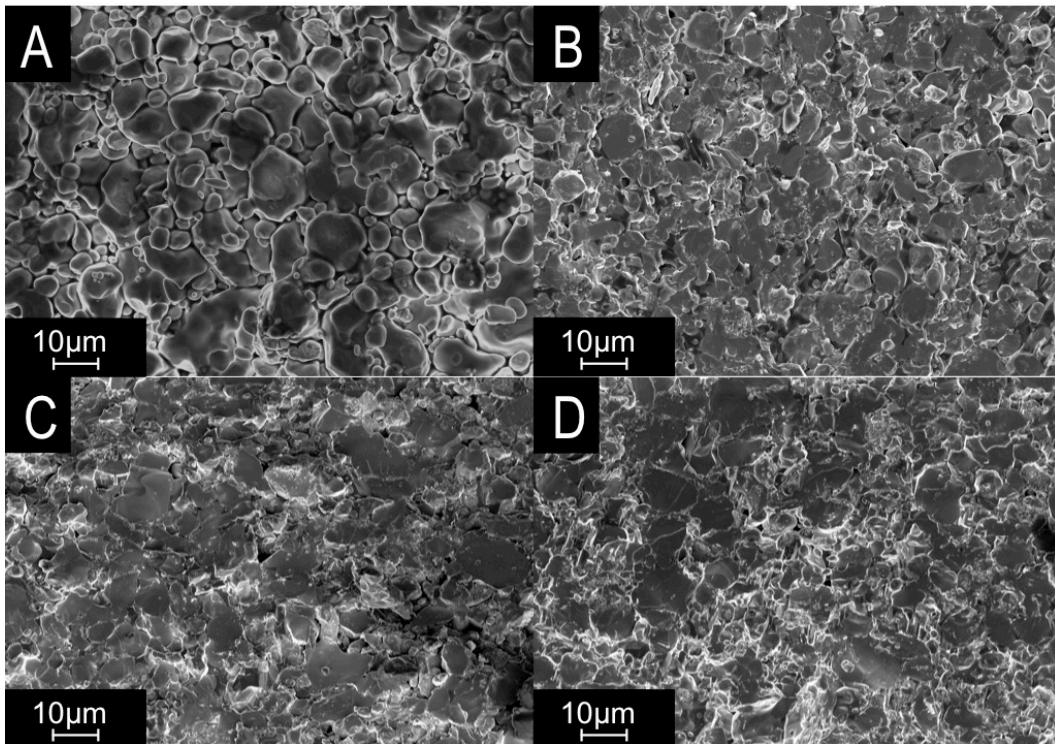


Figure 3.7 SEM fracture surface images (secondary electrons) at 1000x of a) 0 wt% TIB b) 1 wt% TIB c) 2 wt% TIB and d) 5 wt% TIB.

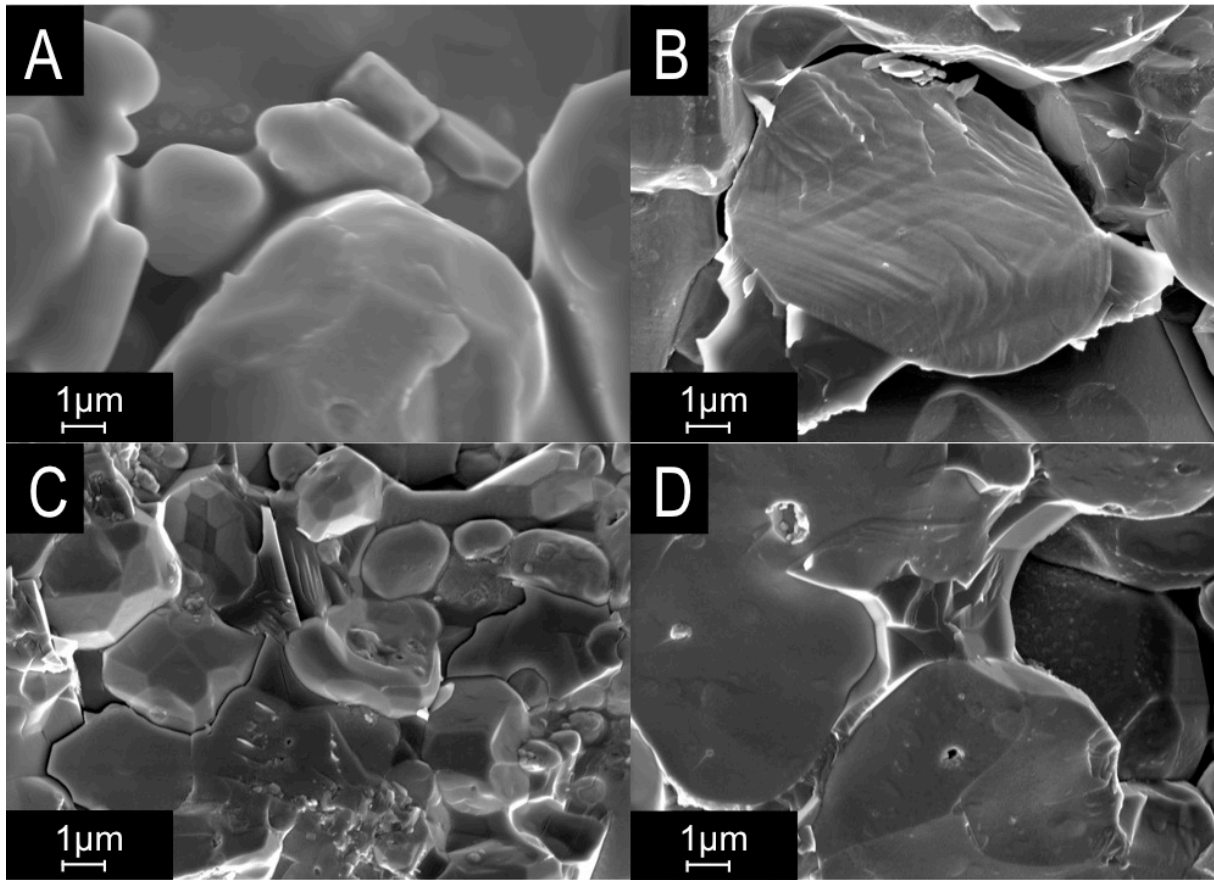


Figure 3.8 SEM fracture surface images (secondary electrons) at 8000x of a) 0 wt% TIB b) 1 wt% TIB c) 2 wt% TIB and d) 5 wt% TIB. It is observed that in the 0 wt% TIB sample, that due to the lack of particle necking sintering did not occur. At 2 wt% TIB, the LLZO particles have changed shape (faceted surfaces) which indicates an intermediate stage of liquid phase sintering. Finally, particle coalescence is observed in the 5wt% TIB sample.

The polished surface SEM images were conducted on all four hot pressed samples after mounting them in epoxy and polishing the surfaces in oil using 50 nm abrasive media. All polished surface images were conducted using secondary and backscattered electrons. Only the backscattered images are included, however, as these more clearly indicate the progression of density with increasing wt% TIB addition (Figure 3.6). The control sample with 0wt% TIB addition exhibits the greatest amount of porosity with an estimated vol% porosity of 24%. There is a clear particle size distribution for the control sample with an estimated particle size range of

1 – 15 μm . All other hot pressed samples in Figure (3.6 b-d) have portions of the surface where the particles have agglomerated and therefore the total vol% of porosity has decreased to 18%, 12%, and 8% for the 1 wt%, 2 wt%, and 5 wt% TIB samples, respectively. The particle size distribution in these samples is not as clear as for the control sample.

The fracture surface images of the hot pressed samples with TIB additions seem consistent with the observations made by Ohta *et al.* (Ohta *et al.* 2013) Their investigation included a 1:1 mixture of lithium cobalt oxide (LCO) and Li_3BO_3 (LBO) screen-printed coating on a solid electrolyte LiLaZrNbO (LLZONb). It is reported that at 700°C , the LBO melted and filled the voids and interface spaces between LCO and LLZONb. (Ohta *et al.* 2013) In the present work, the initial heat treatment of 450°C likely removed the organic material, leaving the boron in the form of B_2O_3 to adhere to the surface of each tetragonal LLZO particle. The bonded B_2O_3 -coated LLZO particles then underwent a second heat treatment at a temperature higher than the LBO melting temperature of 700°C . Therefore it is probable that the hot pressing temperature of 900°C in this work not only melted the B_2O_3 present on the surface of each tetragonal LLZO particle but, once melted, this produced a gradient in concentration that caused excess Li from within the LLZO system to migrate to the surface of each particle and chemically reacted with boron oxide to form a lithium borate phase. This lithium borate phase is considered to be a glassy phase because it conformed to what appeared to be a pore, thus indicating it was likely liquid at one point. Similar observations were made in the LLZO system doped with 1.2 wt% Al_2O_3 by McGinn *et al.* Their findings conclude that “from a [ceramic] processing standpoint the liquid phase that develops as a result of Al additions serves to promote

densification and shorten sintering times”.(Jin & McGinn 2011) In this study it was found that X wt% additions of TIB promoted the densification of LLZO by forming what appeared to be a glassy phase while also decreasing the sintering temperature.

3.3.3 Electrochemical Impedance spectroscopy (EIS)

The impedance spectra of all four hot pressed samples were conducted at RT in the frequency range of 7 MHz to 1 Hz (Figure 3.10 and 3.11). Each pellet was polished and sputtered with Pt as the blocking electrodes. The control sample, with 0 wt% TIB, did not adequately densify to allow for transport properties measurement. For the other hot pressed pellets, X = 1, 2, and 5 wt% TIB, the markers and black lines in Figures 3.10 and 3.11 indicate the experimental results and equivalent circuit model best-fit lines, respectively. Both impedance plots were normalized to the geometrical factor (t/A) where t and A are the thickness and area of the sample, respectively. Table 2 reports the results of the equivalent circuit modeling which includes the Q-values, alpha values, percent grain boundary contribution, and the bulk and total conductivities for all three X wt% TIB samples (Table 3.1). The reported total conductivity is a sum of the bulk and grain boundary contributions. The low frequency Nyquist plot of the three hot pressed samples, X wt% TIB, where X = 1, 2, and 5 is shown in (Figure 3.10) and is consistent with a blocking electrode where the tail approaches a vertical asymptote.

As seen in the XRD results a distinct phase transition from tetragonal to cubic LLZO occurred with the addition of TIB to the X wt% TIB samples. As observed in the SEM micrographs, a secondary phase precipitated at the junctions between solid LLZO particles and is predicted to be a high temperature lithium borate phase. The presence of this lithium borate phase accelerated particle-to-particle contact, caused adjacent LLZO particles to coalesce, and prevented significant grain growth. These events occurred at a lower sintering temperature than

seen in previous hot pressing studies(Rangasamy *et al.* 2012) and resulted in reduced grain boundary resistances for all three hot pressed X wt% TIB pellets (Table 3.1). The low grain boundary resistances enabled measurement of the bulk ionic conductivities at high frequencies (Table 3.1). The Q-values for the bulk and grain boundary for both the hot pressed TIB samples are similar and are relatively consistent with the values expected for the bulk and grain boundary processes.(Huggins 2002; Irvine *et al.* 1990)

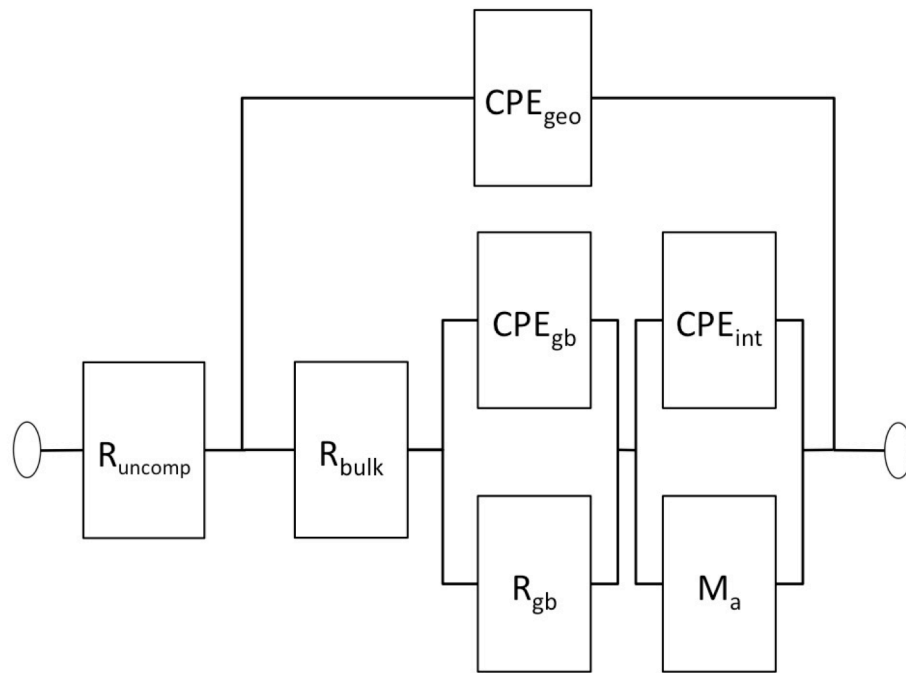


Figure 3.9 Equivalent circuit model based on work by Huggins *et al.*(Huggins 2002) R, CPE, and M refer to the resistance, mass transport element, and constant phase element and the subscripts uncomp, geo, gb, int represent uncompensated, geometric dimensions, grain boundary, and interfaces.

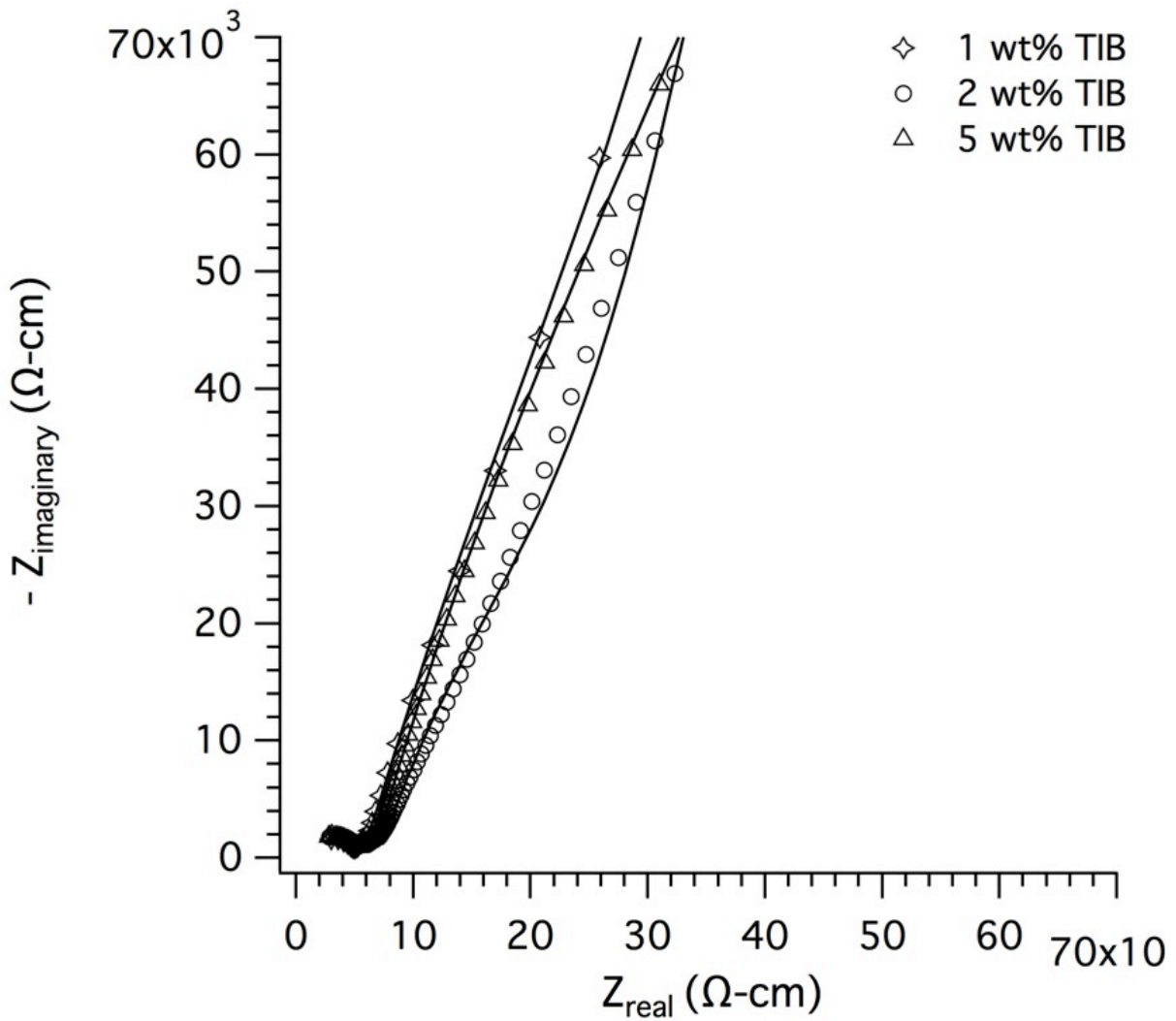


Figure 3.10 Impedance plot (7 MHz – 1 Hz) of hot-pressed LLZO – X wt% TIB pellets. Markers indicate experimental data and the solid lines, for the X = 1, 2, and 5wt% TIB, indicate the equivalent circuit modeled line.

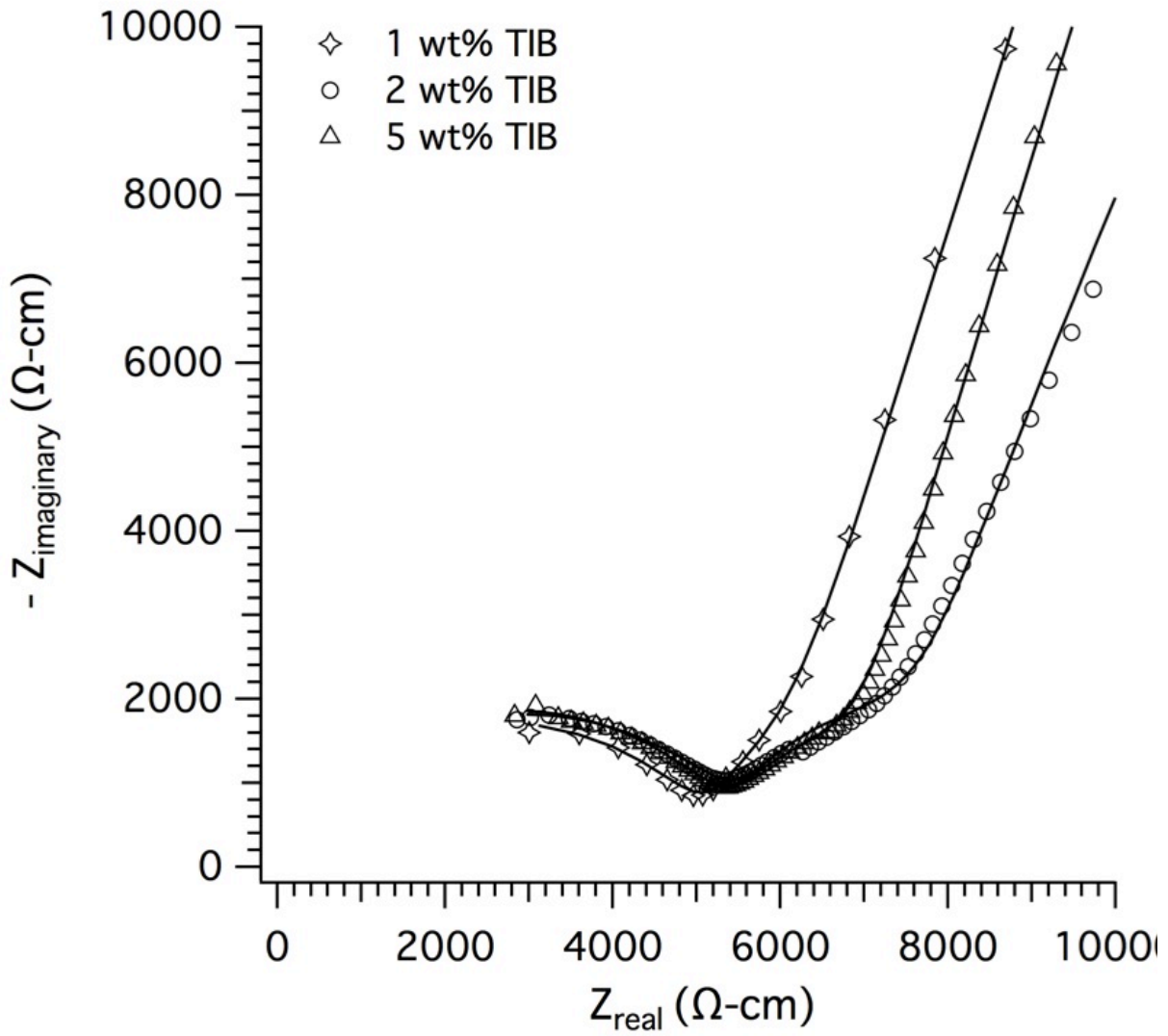


Figure 3.11 Impedance plot of hot-pressed LLZO-Xwt% TIB pellets. Markers indicate experimental data and the solid lines, for the X = 1, 2, and 5wt% TIB, indicate the equivalent circuit modeled line.

| Sample | Q_{bulk} | α_{bulk} | Q_{gb} | α_{gb} | % R_{gb} | σ_{bulk} (mS/cm) | σ_{total} (mS/cm) |
|-------------|-----------------------|------------------------|----------------------|----------------------|-------------------|-----------------------------------|------------------------------------|
| 1wt% TIB | 4.6×10^{-10} | 0.719 | 2.8×10^{-9} | 1.00 | 9% | 0.19 | 0.17 |
| 2wt% TIB | 7.3×10^{-10} | 0.701 | 1.3×10^{-9} | 1.00 | 21% | 0.17 | 0.13 |
| 5wt% TIB | 4.1×10^{-10} | 0.733 | 1.4×10^{-9} | 1.00 | 16% | 0.18 | 0.15 |

Table 3.1 Electrochemical properties of hot pressed LLZO – X wt% TIB where X = 0, 1, 2, and 5wt%. The Q_{gb} , Q_{bulk} , α_{gb} , and α_{bulk} represent the Q-values and α 's for both the grain boundary and bulk. The %grain boundary contribution to the total conductivity is seen here in column 4. The bulk and total conductivities are reported based on values from the best fit data. The total conductivity reported is the sum of the bulk and gb resistivities, normalized by geometric dimensions during equivalent circuit modeling.

3.3.3.1 Effects of the TIB sintering aid

Firstly, excess Li was added to the system to account for the Li loss that occurs during high temperature processing (hot pressing), which was covered in Chapter 2. Synthesizing tetragonal LLZO with 32 wt% excess Li provided a source of Li for the B_2O_3 coating at 900°C . Generally, liquid phase sintering achieves rapid densification because mass transport occurs directly from grain to grain.(Barsoum 2002; German *et al.* 2008) In this case, however, it is probable that Li from within the LLZO grains diffused to the melted B_2O_3 surface. At high temperatures, the Li from the tetragonal LLZO with the B_2O_3 coating formed the lithium borate phase and efficiently surrounded each LLZO particle. German proposed that coating each particle with the sintering aid directly, as opposed to adding small volume fractions of powdered sintering aid, would result in better densification as well as minimizing the amount of secondary phase present at the grain boundaries.(German *et al.* 2008)

Secondly, other groups have investigated pressure-less sintering with sintering aids by introducing Li_3BO_3 in various amounts to LLZO.(Tadanaga *et al.* 2013; Takano *et al.* 2014) Results have indicated that at a 0.68 mol ratio of $\text{Li}_3\text{BO}_3/\text{LLZO}$ (~ 6 wt% Li_3BO_3), the highest total conductivity was achieved. The $\text{Li}_3\text{BO}_3/\text{LLZO}$ composites studied by Tadanaga *et al* and Takano *et al* were both processed similarly by pressure-less sintering cold pressed pellets at 900°C for 36 h and 10 h, respectively.(Tadanaga *et al.* 2013; Takano *et al.* 2014) The electrochemical properties of these $\text{Li}_3\text{BO}_3/\text{LLZO}$ composites were tested and attained estimated total ionic conductivities of $1 \times 10^{-4} \text{ S cm}^{-1}$ and $1.9 \times 10^{-5} \text{ S cm}^{-1}$.(Tadanaga *et al.* 2013; Takano *et al.* 2014) Clearly, pressure-less sintering is highly dependent on sintering time but with respect to the results obtained in this study, hot pressing LLZO with X wt% TIB has attained higher conductivity values in a shorter time (Table 3.2). Though the sintering aid in this study was not added in powder form, it is believed that the B_2O_3 coating (after the initially 450°C heat treatment) formed a lithium borate phase in-situ during the hot pressing step and therefore can also be classified as a lithium borate phase/LLZO composite.

Finally, another significant finding in this study is that the phase transition from tetragonal to cubic occurred during the hot pressing step and not without the addition of at least 1 wt% TIB (Figure 3.4 and 3.5). Though the control sample (LLZO – 0 wt% TIB) was unable to provide any electrochemical results, Takano *et al* report that their LLZO pellet without sintering additives exhibited a total ionic conductivity of $1.6 \times 10^{-5} \text{ S cm}^{-1}$.(Takano *et al.* 2014) The LLZO pellet in their study, however, initially started with cubic LLZO powder, which, as

previously investigated, is the higher conducting phase. In comparison, Awaka *et al* reported $1.63 \times 10^{-6} \text{ S cm}^{-1}$ and $5.59 \times 10^{-7} \text{ S cm}^{-1}$ for the bulk and grain boundary Li-ion conductivity of tetragonal LLZO.(Awaka *et al.* 2009) Therefore, from Figures 3.10, 3.11 and Table 3.1, all of the X wt% TIB (X = 1, 2, and 5) samples in this study exhibit cubic LLZO Li-ion conductivity behavior with two orders of magnitude increase from pure tetragonal LLZO.

3.4 Conclusion

To reduce both the sintering temperature and grain boundary effects, this study examined the impact of introducing boron in the form of tri-isopropyl borate (TIB) into tetragonal LLZO. It has been shown herein that by adding TIB and heating these samples to two different heating cycles, transforms the tetragonal LLZO powder to a cubic phase while also forming an in-situ lithium borate phase between the grains. Solid state $\text{Li}_{6.22}\text{La}_3\text{Zr}_2\text{Al}_{0.26}\text{O}_{12}$ (LLZO) + 32 wt% ex Li_2CO_3 garnet powder was synthesized and confirmed to be the tetragonal phase by powder X-Ray diffraction (XRD). In this study a novel technique to process LLZO with a sintering aid was used to form a lithium borate phase in-situ between the LLZO grains during hot pressing. The formation of this lithium borate secondary phase at the grain boundaries and triple points produced a the gradient of the liquid boron at the surface of the LLZO grains, which possibly led in turn to the diffusion of mobile Li out of the tetragonal LLZO powder to form the lithium borate phase. The tetragonal phase of LLZO was successfully converted to cubic LLZO and confirmed via powder XRD. This is the first time LLZO was sintered to 8 vol% porosity at a relatively low temperature (900°C) for a relatively low time (1 h). This was made possible with a small addition of a sintering aid, which functioned as a liquid phase sintering mechanism during processing. The boron source was added in liquid form and chemically bonded to LLZO particle

surfaces during the first heat treatment of 450°C. After the second heat treatment at 900°C the highest ionic conductivity of 0.17 mS cm⁻¹ was found for the LLZO – 1 wt% TIB sample.

4. Future Works

This work discussed enabling a shift in the use of hazardous liquid electrolytes in LIBs to a solid ceramic material. In general, the future of LIBs for EV applications relies on improving the electrode materials and the electrolyte to achieve greater specific energies, but there are still many hurdles to overcome before solid electrolytes can attain the same ionic conductivity values as their liquid counterparts. For the LLZO solid electrolyte system, achieving this goal will depend on developing new processing methods that will create materials near theoretical density without the need for high sintering temperatures. The present work has made progress on this front, which indicates that further investigation into this approach may yield additional gains. For example, follow up experiments can be performed to determine the optimum sintering times and sample thicknesses needed to produce high density samples, as well as to better understand the mechanics of the liquid phase sintering effects discussed in Chapter 3.

The temperature reduction that has been reported in Chapter 3 is a practical benefit that will lend itself well to manufacturing this solid electrolyte for industrial purposes. The temperature is just one of many variables (e.g. initial particle size and sintering time) that must be studied to determine the optimal sintering conditions of the LLZO + TIB system. Two possible follow-up experiment related to this would be 1) a hot-pressing study under constant pressure and temperature where the sintering time is varied in 15 min increments; and 2) preparing samples with different initial particle sizes. The results of such studies would be helpful in identifying the best sintering conditions for these materials. Conducting similar

characterization techniques with XRD, SEM, EIS, and eventually cyclic voltammetry would illuminate the salient features of this system.

Processing LLZO + TIB in new ways to advance this technology towards large-scale manufacturing will require the capability to manufacture large numbers of specimens at once. The next step beyond hot pressing, which is as most a three-sample-per-run process, will be to involve pressure-less sintering as an alternative. Several SCO electrolyte systems have been investigated for their ionic conductivity by tape casting a paste-like suspension, which consists of a solvent, dispersant, binder, plasticizer, and the SCO powder. This paste is cast onto a metallic or polymer substrate using a mechanical blade and the paste thickness can vary from 10 to 1000 μm .(Meier *et al* 2004) Once dried, this green body can be flexible and will need to be sintered to achieve the necessary electrochemical properties. For the LLZO + TIB SCO electrolyte system, promising results have shown that using binders such as cellulose methyl carboxylate (CMC) and plasticizers such as styrene butadiene rubber (SBR) suspend the LLZO particles in a paste and allow a slurry to be tape cast as a $<150 \mu\text{m}$ film. More research is necessary to avoid the main hindrance associated with tape casting, which are the cracks that form during drying.

BIBLIOGRAPHY

BIBLIOGRAPHY

- Allen, J.L. et al., 2012. Journal of Power Sources. *Journal of Power Sources*, 206, pp.315–319.
- Anon, 2012. *Estimated U.S. Energy use in 2011: ~97.3 Quads*, LLNL. Available at: https://flowcharts.llnl.gov/content/energy/energy_archive/energy_flow_2011/LLNLUSEnergy2011.png [Accessed May 22, 2014].
- Aono, H., 1990. Ionic Conductivity of Solid Electrolytes Based on Lithium Titanium Phosphate. *Journal of The Electrochemical Society*, 137(4), p.1023.
- Aono, H. et al., 1991. Electrical property and sinterability of $\text{LiTi}_2(\text{PO}_4)_3$ mixed with lithium salt (Li_3PO_4 or Li_3BO_3). *Solid State Ionics*, 47, pp.257–264.
- Aono, H., Sugimoto, E. & Sadaoka, Y., 1990. Ionic Conductivity of $\text{LiTi}_2(\text{PO}_4)_3$ Mixed with Lithium Salts. *Chemistry Letters*, 3, pp.331–334.
- Awaka, J. et al., 2011. Crystal Structure of Fast Lithium-ion-conducting Cubic $\text{Li}_7\text{La}_3\text{Zr}_2\text{O}_{12}$. *Chemistry Letters*, 40(1), pp.60–62.
- Awaka, J. et al., 2009. Synthesis and structure analysis of tetragonal $\text{Li}_7\text{La}_3\text{Zr}_2\text{O}_{12}$ with the garnet-related type structure. *Journal of Solid State Chemistry*, 182(8), pp.2046–2052.
- Ban, C.W. & Choi, G.M., 2001. The effect of sintering on the grain boundary conductivity of lithium lanthanum titanates. *Solid State Ionics*, 140, pp.285–292.
- Barsoum, 2002. *Fundamentals of Ceramics*, CRC Press.
- Bate, J.B. et al., 2002. Electrical properties of amorphous lithium electrolyte thin films. *Solid State Ionics*, 53-56, pp.647–654.
- Bellekom, S. et al., 2012. Electric cars and wind energy: Two problems, one solution? A study to combine wind energy and electric cars in 2020 in The Netherlands. *Energy*, 45(1), pp.859–866.
- Bruce, P.G. et al., 2011. Li–O₂ and Li–S batteries with high energy storage. 11(1), pp.19–29.
- Budde-Meiwes, H. et al., 2013. A review of current automotive battery technology and future prospects. *Proceedings of the Institution of Mechanical Engineers, Part D: Journal of Automobile Engineering*, 227(5), pp.761–776.
- Burke, A. & Miller, M., 2011. Journal of Power Sources. *Journal of Power Sources*, 196(1), pp.514–522.
- Buschmann, H. et al., 2011. Structure and dynamics of the fast lithium ion conductor " $\text{Li}_7\text{La}_3\text{Zr}_2\text{O}_{12}$." *Physical Chemistry Chemical Physics*, 13(43), p.19378.

- Chu, Y.S., 2007. Basic Research Needs for Electrical Energy Storage: Report of the Basic Energy Sciences Workshop on Electrical Energy Storage. pp.1–186.
- Committee on Climate Change, C., 2012. Cost and performance of EV batteries. pp.1–100.
- De Jonghe, L.C., 1979. Grain boundaries and ionic conduction sodium beta alumina. *Journal of Materials Science*, 14, pp.33–48.
- Dunn, B., Kamath, H. & Tarascon, J.M., 2011. Electrical Energy Storage for the Grid: A Battery of Choices. *Science*, 334(6058), pp.928–935.
- Fang, Z.Z., 2010. *Sintering of Advanced Materials*, Elsevier.
- Galli, S., Scaglione, A. & Wang, Z., 2011. For the Grid and Through the Grid: The Role of Power Line Communications in the Smart Grid. *Proceedings of the IEEE*, 99(6), pp.998–1027.
- Gellert, M. et al., 2012. Grain Boundaries in a Lithium Aluminum Titanium Phosphate-Type Fast Lithium Ion Conducting Glass Ceramic: Microstructure and Nonlinear Ion Transport Properties. *The Journal of Physical Chemistry C*, 116(43), pp.22675–22678.
- German, R.M., Suri, P. & Park, S.J., 2008. Review: liquid phase sintering. *Journal of Materials Science*, 44(1), pp.1–39.
- Goodenough, J.B., 1984. Review Lecture: Fast ionic conduction in solids. *Proceedings of the Royal Society A*, 393, pp.215–234.
- Goodenough, J.B. & Kim, Y., 2010. Challenges for Rechargeable Li Batteries †. *Chemistry of Materials*, 22(3), pp.587–603.
- Goodenough, J.B. & Park, K.-S., 2013. The Li-Ion Rechargeable Battery: A Perspective. *Journal of the American Chemical Society*, 135(4), pp.1167–1176.
- Hagman, L.-O. & Kierkegaard, P., 1968. The Crystal Structure of $\text{NaMe}_2^{\text{IV}}(\text{PO}_4)_3$; $\text{Me}^{\text{IV}} = \text{Ge}, \text{Ti}, \text{Zr}$. *Acta Chemica Scandinavica*, pp.1822–1832.
- Hashmi, M., Hänninen, S. & Mäki, K., 2011. Survey of Smart Grid Concepts, Architectures, and Technological Demonstrations Worldwide. *IEEE*, pp.1–7.
- Hong, H.Y.-P., 1978. Crystal Structure and ionic conductivity of $\text{Li}_{14}\text{Zn}(\text{GeO}_4)_4$ and other new Li^+ superionic conductors. *Material Research Bulletin*, 13, pp.117–124.
- Hsieh, M.Y. & DeJonghe, L.C., 1978. Silicate-Containing Sodium Beta-Alumina Solid Electrolytes. *Journal of the American Ceramic Society*, 61, pp.185–191.
- Hu, Y.-W., Raistrick, I.D. & Huggins, R.A., 1976. Ionic Conductivity of Lithium photophosphate-doped Lithium orthosilicate. *Material Research Bulletin*, 11, pp.1227–1230.

- Huang, M. et al., 2011. Effect of sintering temperature on structure and ionic conductivity of $\text{Li}_{7-x}\text{La}_3\text{Zr}_2\text{O}_{12-0.5x}$ ($x = 0.5\sim 0.7$) ceramics. *Solid State Ionics*, pp.1–5.
- Huggins, R.A., 2002. Simple Method to Determine Electronic and Ionic Components of the Conductivity in Mixed Conductors A Review. *Ionics*, 8.3-4, pp.300–313.
- Inaguma, Y. et al., 1994. Candidate compounds with perovskite structure for high lithium ionic conductivity. *Solid State Ionics*, 70/71, pp.196–202.
- Irvine, J.T.S., Sinclair, D.C. & West, A.R., 1990. Electroceramics: Characterization by Impedance Spectroscopy. *Advanced Materials*, 2(3), pp.132–138.
- Ishiguro, K. et al., 2013. Stability of Nb-Doped Cubic $\text{Li}_7\text{La}_3\text{Zr}_2\text{O}_{12}$ with Lithium Metal. *Journal of The Electrochemical Society*, 160(10), pp.A1690–A1693.
- Jackman, S.D. & Cutler, R.A., 2012. Effect of microcracking on ionic conductivity in LATP. *Journal of Power Sources*, 218(C), pp.65–72.
- Jin, Y. & McGinn, P.J., 2011. Al-doped $\text{Li}_7\text{La}_3\text{Zr}_2\text{O}_{12}$ synthesized by a polymerized complex method. *Journal of Power Sources*, 196(20), pp.8683–8687.
- Jones, B.E., 1911. *Electric Primary batteries; a practical guide to their construction and use*, Cassell and Company, Ltd.
- Kanno, R. et al., 2000. Synthesis of a new lithium ionic conductor, thio-LISICON–lithium germanium sulfide system. *Solid State Ionics*, 130, pp.97–104.
- Kingery, W.D., 1963. Effects of Applied Pressure on Densification During Sintering in the Presence of a Liquid. *Journal of the American Ceramic Society*, 46(8), pp.391–395.
- Kingery, W.D., 1960. *Introduction to Ceramics*,
- Kley, F., Lerch, C. & Dallinger, D., 2011. Energy Policy. *Energy Policy*, 39(6), pp.3392–3403.
- Knauth, P., 2009. Inorganic solid Li ion conductors: An overview. *Solid State Ionics*, 180(14-16), pp.911–916.
- Kumazaki, S. et al., 2011. Electrochemistry Communications. *Electrochemistry Communications*, 13(5), pp.509–512.
- Kurzweil, P., 2009. Secondary Batteries. *Elsevier B.V*, pp.565–578.
- Li, Yiqiu, Cao, Y. & Guo, X., 2013. Solid State Ionics. *Solid State Ionics*, 253(C), pp.76–80.
- Li, Yutao et al., 2012. Ionic distribution and conductivity in lithium garnet $\text{Li}_7\text{La}_3\text{Zr}_2\text{O}_{12}$. *Journal of Power Sources*, 209, pp.278–281.
- Mariappan, C.R. et al., 2011. Correlation between micro-structural properties and ionic conductivity of $\text{Li}_{1.5}\text{Al}_{0.5}\text{Ge}_{1.5}(\text{PO}_4)_3$ ceramics. *Journal of Power Sources*, 196(15), pp.6456–

6464.

- Mathews, M.D., Tyagi, A.K. & Moorthy, P.N., 1998. High-temperature behaviour of lithium borates: Part I: Characterization and thermal stability. *Thermochimica Acta*, 320, pp.89–95.
- Monroe, C. & Newman, J., 2005. The Impact of Elastic Deformation on Deposition Kinetics at Lithium/Polymer Interfaces. *Journal of The Electrochemical Society*, 152(2), p.A396.
- Murugan, R., Thangadurai, V. & Weppner, W., 2007. Fast Lithium Ion Conduction in Garnet-Type $\text{Li}_7\text{La}_3\text{Zr}_2\text{O}_{12}$. *Angewandte Chemie International Edition*, 46(41), pp.7778–7781.
- Naziripour, G.A. et al., 1985. Hot-pressed polycrystalline yttrium iron garnet. *Journal of Materials Science*, 20, pp.375–380.
- Ohta, S. et al., 2013. Journal of Power Sources. *Journal of Power Sources*, 238(C), pp.53–56.
- Ohta, S., Kobayashi, T. & Asaoka, T., 2011. High lithium ionic conductivity in the garnet-type oxide $\text{Li}_{7-x}\text{La}_3(\text{Zr}_{2-x}, \text{Nb}_x)\text{O}_{12}$ ($x = 0-2$). *Journal of Power Sources*, 196(6), pp.3342–3345.
- Rangasamy, E., Wolfenstine, J. & Sakamoto, J., 2012. The role of Al and Li concentration on the formation of cubic garnet solid electrolyte of nominal composition $\text{Li}_7\text{La}_3\text{Zr}_2\text{O}_{12}$. *Solid State Ionics*, 206(C), pp.28–32.
- Roberston, A.D., West, A.R. & Ritchie, A.G., 1997. Review of crystalline lithium-ion conductors suitable for high temperature battery applications. *Solid State Ionics*, 104, pp.1–11.
- Rousse, G., Baptiste, B. & Lelong, G., 2014. Crystal Structures of $\text{Li}_6\text{B}_4\text{O}_9$ and $\text{Li}_3\text{B}_{11}\text{O}_{18}$ and Application of the Dimensional Reduction Formalism to Lithium Borates. *Inorganic Chemistry*, p.140519010045006.
- Sakamoto, J., 2012. *Keeping up with the demands for electrochemical energy storage*, The Bridge.
- Sastry, B.S.R. & Hummel, F.A., 1959. Studies in Lithium Oxide Systems: V, $\text{Li}_2\text{O}-\text{Li}_2\text{O}^* \text{B}_2\text{O}_3$. *Journal of the American Ceramic Society*, 42(5), pp.216–218.
- Shimonishi, Y. et al., 2011. Synthesis of garnet-type $\text{Li}_{7-x}\text{La}_3\text{Zr}_2\text{O}_{12-1/2x}$ and its stability in aqueous solutions. *Solid State Ionics*, pp.1–6.
- Song, M.-K., Zhang, Y. & Cairns, E.J., 2013. A Long-Life, High-Rate Lithium/Sulfur Cell: A Multifaceted Approach to Enhancing Cell Performance. *4.30.2014 Thesis Introduction Sections 1.5 - 1.7*, 13(12), pp.5891–5899.
- Tadanaga, K. et al., 2013. Low temperature synthesis of highly ion conductive $\text{Li}_7\text{La}_3\text{Zr}_2\text{O}_{12}-\text{Li}_3\text{BO}_3$ composites. *Electrochemistry Communications*, 33, pp.51–54.
- Takano, R. et al., 2014. Low temperature synthesis of Al-doped $\text{Li}_7\text{La}_3\text{Zr}_2\text{O}_{12}$ solid electrolyte

- by a sol–gel process. *Solid State Ionics*, 255(C), pp.104–107.
- Tamura, S., Nobuhito, I. & Adachi, G.-Y., 1999. Ceramics Sinterability Enhancement at Ambient Pressure by Boron Oxide Addition. *Advanced Materials*, 11(1), pp.64–66.
- Tarascon, J.M. & Armand, M., 2001. Issues and challenges facing rechargeable lithium batteries. *Nature*, 414, pp.359–367.
- Teng, S., Tan, J. & Tiwari, A., 2014. Recent developments in garnet based solid state electrolytes for thin film batteries. *Current Opinion in Solid State and Materials Science*, 18(1), pp.29–38.
- Thangadurai, V., Kaack, H. & Weppner, W., 2003. Novel Fast Lithium Ion Conduction in Garnet-Type $\text{Li}_5\text{La}_3\text{M}_2\text{O}_{12}$ (M = Nb, Ta). *Journal of the American Ceramic Society*, 86(3), pp.437–430.
- van Vliet, O. et al., 2011. Energy use, cost and CO_2 emissions of electric cars. *Journal of Power Sources*, 196(4), pp.2298–2310.
- van Vliet, O.P.R. et al., 2010. Techno-economic comparison of series hybrid, plug-in hybrid, fuel cell and regular cars. *Journal of Power Sources*, 195(19), pp.6570–6585.
- Virkar, A.V., Ketcham, T.D. & Gordon, R.S., 1979. Hot Pressing of Lithia-Stabilized Beta"-Alumina. *Ceramurgia International*, 5(2), pp.1–4.
- Volta, A., 1800. *On the Electricity Excited by the Mere Contact of Conducting Substance of Different Kinds*, Phil. Trans. R. Soc. Lond.
- Wachsman, E.D. & Lee, K.T., 2011. Lowering the Temperature of Solid Oxide Fuel Cells. *Science*, 334(6058), pp.935–939.
- Wolfenstine, J. et al., 2010. Journal of Power Sources. *Journal of Power Sources*, 195(13), pp.4124–4128.
- Wolfenstine, J. et al., 2013. Materials Letters. *Materials Letters*, 96(C), pp.117–120.
- Wolfenstine, J., Sakamoto, J. & Allen, J.L., 2012. Electron microscopy characterization of hot-pressed Al substituted $\text{Li}_7\text{La}_3\text{Zr}_2\text{O}_{12}$. *Journal of Materials Science*, 47(10), pp.4428–4431.
- Wong, D.T. et al., 2012. J. Mem. Sci., 181, pp. 175.
- Yu, X. et al., 1997. A Stable Thin-Film Lithium Electrolyte: Lithium Phosphorus Oxynitride. *J. of Electrochem. Soc.*, 144(2), pp.524–532.